ABSTRACT

Name: Andriy Zatserklyaniy Department: Physics

Title: A Search for Third Generation Scalar Leptoquarks

Major: Physics Degree: Doctor of Philosophy

Approved by: Date:

Dissertation Director

NORTHERN ILLINOIS UNIVERSITY

ABSTRACT

Leptoquarks (LQ) are particles with both color and lepton number predicted in some gauge theories and composite models. Current theory suggests that leptoquarks would come in three different generations. We report on a search for charge 1/3 third generation leptoquarks produced in $p\bar{p}$ collisions at $\sqrt{s}$=1.96 TeV using data collected by the D0 detector at Fermilab. Such leptoquarks would decay into a tau-neutrino plus a b-quark with branching fraction B. We present preliminary results on an analysis where both leptoquarks decay into neutrinos giving a final state with missing energy and two b-jets. Using 425(recorded) pb^{-1} of data, we place limits on $\sigma(p\bar{p} \rightarrow LQ\overline{LQ})B^2$ as a function of the leptoquark mass. Assuming $B = 1$, we excluded at the 95% confidence level scalar third generation leptoquarks with $M_{LQ} < 219$ GeV.

NORTHERN ILLINOIS UNIVERSITY

A SEARCH FOR THIRD GENERATION SCALAR LEPTOQUARKS

A DISSERTATION SUBMITTED TO THE GRADUATE SCHOOL
IN PARTIAL FULFILLMENT OF THE REQUIREMENTS
FOR THE DEGREE
DOCTOR OF PHILOSOPHY

DEPARTMENT OF PHYSICS

BY

ANDRIY ZATSERKLYANIY

DEKALB, ILLINOIS

2006

Certification:

In accordance with departmental and Graduate School policies, this dissertation is accepted in partual fulfillment of degree requirements

Dissertation Director

Date

DEDICATION

To Tanya

ACKNOWLEDGEMENTS

I would like to thank my advisor, David Hedin. He corrected a million errors in this document. I am grateful to Arthur Maciel for his assistance and support. I would like to thank Steven Martin for his excellent introduction to quantum field theory and supersymmetry. I thank Sergey Uzunyan and Mikhail Arov for discussion of numerous physics questions.

I thank all members of DØ and the Tevatron staff; they made this work possible. I am especially grateful to members and convenors of DØ New Phenomena group for their friendly and useful comments and suggestions. I would like to thank Arnaud Duperrin and Patrice Verdier for fruitful discussions. I thank Pushpa Bhat for her interest in this work.

I would like to acknowledge the financial support of the National Science Foundation.

TABLE OF CONTENTS

Chapter Page

Chapter Page

LIST OF TABLES

LIST OF FIGURES

Figure Page

Figure Page

CHAPTER 1
INTRODUCTION

1.1 The Standard Model of Particle Physics

The macroscopic world around us is built out of particles. Under some conditions we can define elementary particles as quantum mechanical objects having certain properties. Thus, this definition is valid for a number of objects, e.g. electron, pion, atom. We can narrow our definition by a rather vague requirement for the "true" elementary particle to not manifest any internal structure. Under this agreement, the basic building blocks of matter are fermions, leptons and quarks, which interact by means of exchanging vector bosons. The masses and electric charges of quarks and leptons are listed in Table 1.1; each row represents the generation of the particles.

Table 1.1: The known quarks and leptons.

Quarks				Leptons			
Charge 2/3		Charge $-1/3$		Charge -1		Charge 0	
	Mass, GeV		Mass, GeV		Mass, GeV		Mass
u	0.001–0.005	d	0.003–0.009	e	0.000511	ν_e	< 3 eV
c	1.15–1.35	s	0.075–0.175	μ	0.106	ν_μ	< 190 keV
t	174.3 ± 5.1	b	4.0–4.4	τ	1.777	ν_τ	< 18.2 MeV

The vast majority of experimental particle physics facts is described by the Standard Model (SM). The Standard Model is a field theory built from Quantum Mechanics and Relativity Theory. The Lagrangian of the Standard Model is invariant with respect to local gauge transformations.

To represent empirical facts, the Standard Model is based on the symmetry group $SU(3)_c \otimes SU(2)_L \otimes U(1)_Y$. The subgroup $SU(2)_L$ reflects the fact that left- and right-handed particles behave differently in weak interactions. Each kind of lepton or quark is represented in the Lagrangian by two fields: left and right. Left-handed fermions form doublets of leptons

$$\begin{pmatrix} \nu_e \\ e_L \end{pmatrix} \begin{pmatrix} \nu_\mu \\ \mu_L \end{pmatrix} \begin{pmatrix} \nu_\tau \\ \tau_L \end{pmatrix}$$

and quarks

$$\begin{pmatrix} u_L \\ d_L \end{pmatrix} \begin{pmatrix} c_L \\ s_L \end{pmatrix} \begin{pmatrix} t_L \\ b_L \end{pmatrix}$$

The $SU(2)_L$ group transforms the components of doublets into each other. Right-handed fermions

$$e_R, \mu_R, \tau_R, u_R, c_R, t_R, d_R, s_R, b_R$$

are singlets and invariants with respect to $SU(2)_L$ transformations. The only exclusion is neutrinos, which are supposed to be left-handed only. Because the handness is invariant for only massless particles, fields in the Standard Model Lagrangian are massless. The mediating vector fields are massless too. The absence of the explicit mass terms in the Lagrangian also helps the theory to be *renormalizable*. However, fermions other than neutrinos as well as W and Z bosons have mass. To introduce the masses, the Standard Model uses the mechanism of a $soft$ *spontaneous* breaking

of the gauge symmetry, the Higgs mechanism. Here, $soft$ means an absence of mass terms in the Lagrangian. The basic property of the *spontaneous* symmetry breaking is that some symmetry of the Lagrangian is absent in the stable state of the physical vacuum after the breaking. The initial symmetric state should be unstable for spontaneus transition under infinitesimal influences. The spontaneous breaking of the gauge symmetry can be achieved by introducing into the Lagrangian a doublet of scalar fields bearing a weak hypercharge. The resulting potential should be chosen in such a way that the initial state will have a non-zero vacuum expectation value and become unstable. After breaking the symmetry $SU(2)_L \otimes U(1)_Y \rightarrow U(1)_{EM}$ and the vector gauge boson fields W, Z will obtain masses. The $U(1)_{EM}$ symmetry remains unbroken, which constitutes electric charge conservation. The charged leptons and the quarks will obtain masses through Yukawa coupling, while neutrinos, being left-handed only, remain massless. The W boson interactions with quarks results in the Cabibbo-Kobayashi-Maskawa (CKM) mixing matrix.

The subgroup $SU(3)_c$ describes a gauge symmetry under color transformations. The eight generators correspond to the eight gluons, which are massless vector bosons. This symmetry is exact and remains unbroken.

The Standard Model has been built "by hand" to satisfy the experimental facts. The origin some of its features remains unexplained. It is based on 19 parameters which include subgroups' coupling constants, masses of fermions, vector bosons and the Higgs boson, values of the quark-mixing angles and the phase of the CKM matrix. Recent evidence of neutrino mixing will require new parameters. The mechanism of the spontaneous symmetry breaking should be confirmed by

the observation of the scalar particle, the Higgs boson. Therefore, the Standard Model does not look like the final theory. Attempts to extend the Standard Model have been developed in a few directions. Examples are supersymmetric models and Grand Unification Theories (GUT).

CHAPTER 2
LEPTOQUARKS

There are some symmetries between the quarks and leptons of the Standard Model. All of them are grouped into generations. Transitions between generations are nominally forbidden for leptons and highly suppressed for quarks. This symmetry inspires an idea of possible lepton-quark transformations and postulates the existence of particles called leptoquarks (LQ). Leptoquarks, the carriers of such transformations, should have both leptonic and baryonic quantum numbers, fractional electric charge and an integer spin. Also, one assumes that leptoquark interactions are invariant under the Standard Model gauge group $SU(3)_c \otimes SU(2)_L \otimes U(1)_Y$. Most phenomenological models developed for existing colliders assume that leptoquarks preserve generations. This generalization is called the "kinship hypothesis." In other words, it is assumed that all interfamily transitions are suppressed by appropriate small mixing angles. Thus can be forbidden processes involving flavor-changing neutral currents, which are severely constrained [1]. So there will be first, second or third generation leptoquarks which only decay to leptons + quarks of the same generation.

In supersymmetric models scalar squarks can have Yukawa couplings to SM quarks and leptons. These terms being present in the superpotential results in lepton-quark transitions with violation of the leptonic and the baryonic numbers

[2]. The only way to prevent such leptoquark-type transitions is a requirement for the theory to conserve so-called R-parity. This is defined for each particle with a spin s as a multiplicative quantum number

$$P_R = (-1)^{3(B-L)+2s}$$

R-parity conservation requires every term in the superpotential to have $P_R = +1$. The Standard Model particles, including the Higgs boson, have $P_R = +1$, while all supersymmetric particles have $P_R = -1$. The consequences of R-parity conservation are pair production of the sparticles at colliders and the existence of a stable lightest supersymmetric particle (LSP). The non-observation of proton decay (the measured proton lifetime exceeds 10^{33} years) is a strong argument against R-parity violation models. So current SUSY models tend not to predict low mass leptoquarks.

Efforts were undertaken to include $SU(3)_c \otimes SU(2)_L \otimes U(1)_Y$ symmetry in a higher symmetry. The next level of generalization is based on the $SU(5)$ group. The symmetry groups of the Standard Model will be a result of $SU(5)$ spontaneous symmetry breaking. In frames of the unified symmetry $SU(5)$, all interactions will be described before breaking by only one constant. $SU(5)$ itself predicts new fermions, which comprise five-component spinors and gauge bosons. Half of its 24 gauge bosons are the bosons of the Standard Model. The rest are specific for $SU(5)$ bosons, which transform quarks to leptons. They carry fractional charge and violate baryon and lepton numbers. The X-bosons, which carry electric charge $\pm\frac{4}{3}$, transforms quarks to leptons. The Y-bosons with charge $\pm\frac{1}{3}$ conduct transitions from quarks to neutrinos. Their masses should be about the GUT scale, $m_X \approx m_Y \approx 10^{15}$ GeV; again the proton decay lifetime sets constraints on lower mass

leptoquark-like particles.

The Pati-Salam unification model [3] also predicts leptoquark states. It is based on the symmetry group $SU(4)$ which breaks into $SU(3)_c \times U(1)_{B-L}$. The model predicts vector bosons carrying baryonic and leptonic numbers with hypercharge $\frac{2}{3}$ which are singlets with respect to the weak group. These states should be heavy, with mass corresponding to the $SU(4)$ breaking scale.

2.1 Phenomenological Models of Leptoquarks

The GUT and supersymmetric models predict leptoquark states with very high mass, unreachable for contemporary colliders. Nevertheless, there exist some models [4][5] containing leptoquarks which conserve lepton and baryon numbers and possibly exist in the mass range below 1 TeV. In models where baryon and lepton number are separately conserved, leptoquarks can be light (of order the electroweak scale) and still avoid conflicts with rapid proton decay.

Having integer spin, the leptoquark can be either scalar or vector. The fermionic number of the leptoquarks

$$F = 3B + L$$

can be 0 or ± 2. The leptoquarks are color triplets under $SU(3)_c$. It is also assumed that leptoquarks couple either to left- or right-handed leptons. The possible quantum numbers of the leptoquarks [6] are listed in Table 2.1. A subscript denotes the weak isospin of the scalar (S) and vector (V) states; leptoquarks form isospin singlets or multiplets. A tilde differentiates leptoquarks with different hypercharge. Leptoquarks with $F = 2$ (both scalar and vector) couple to lepton-quark, while the leptoquarks with $F = 0$ have lepton-antiquark coupling.

The Lagrangian includes all scalar and vector states.

$$\mathcal{L}_{\text{eff}} = \mathcal{L}_{\text{S}} + \mathcal{L}_{\text{V}}$$

The gauge coupling of the leptoquarks in the Lagrangian are completely determined, while the Yukawa couplings to fermions remain unknown. Different models commonly use Yang-Mills or minimal vector couplings. High energy collider searches put constraints on the leptoquark masses and coupling constants.

2.2 Leptoquark Production on Tevatron

Leptoquarks can be produced at the Tevatron either singly or in pairs. Leptoquarks can be produced singly via $qg \rightarrow LQ + l$. Thus the cross-section of the single production depends on an unknown Yukawa coupling at the leptoquark-quark-lepton vertex. This coupling constant should be small [1], so we will consider pair production only. Fig. 2.1 shows leading order diagrams for leptoquark pair production at the Tevatron [7].

Because leptoquarks are color triplets, the cross-section of their pair production through gluon fusion or quark annihilation can be calculated. The value of the cross-section for scalar leptoquark production depends on the leptoquark mass. The quark-antiquark annihilation dominates the total cross-section for leptoquark masses above 100 GeV [8]. The leading order cross-section for the pair production of scalar leptoquarks via quark-antiquark annihilation is [7]

$$\sigma_{LO}(q\bar{q} \rightarrow LQ\overline{LQ}) = \frac{2\pi\alpha_s^2}{27\hat{s}}\left(1 - \frac{4M_{LQ}^2}{\hat{s}}\right)^{3/2}$$

Calculations of the cross-section for the pair production of vector leptoquarks is performed under assumptions made for a Yukawa coupling. The subject of the

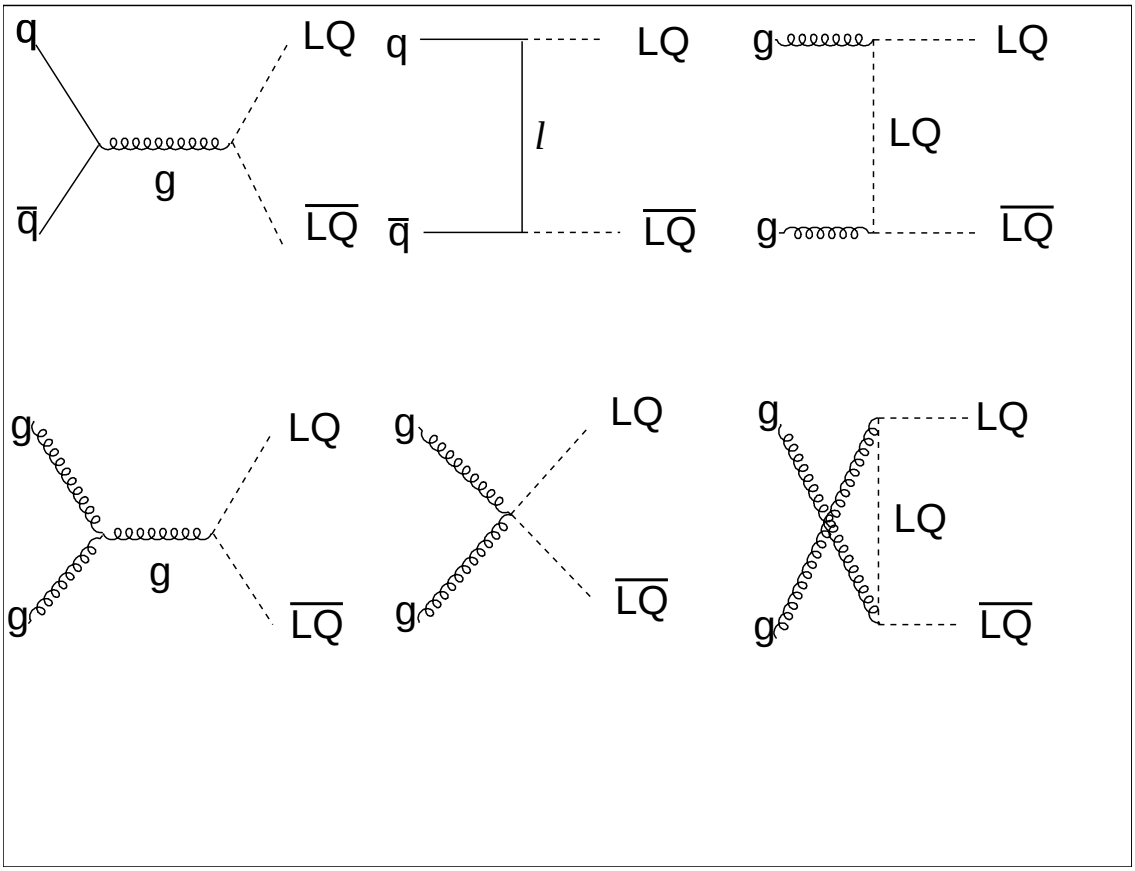

Figure 2.1: Leading-order Feynman diagrams for leptoquark pair production at the Tevatron. The dashed lines represent both scalar and vector leptoquarks.

current study is the pair production of scalar leptoquarks of the third generation. We will use the production cross-sections calculated in [4].

Third generation leptoquarks with charge $\frac{1}{3}$ will decay either to $\nu_\tau b$ or to τt pairs. The second decay channel become possible for $M_{LQ} > M_t + M_\tau$. Even in this case, its branching fraction (B) will be highly suppressed for M_{LQ} close to the threshold [16]. The current search was performed for the first decay channel. Thus, the experimental signature of the decay of a leptoquark pair chosen for this study is the presence of two b-jets and substantial missing transverse energy coming from the neutrinos. Current limits [9][10] on the masses of scalar leptoquarks are listed in Table 2.2. The obtained mass limits depend on B_l, the branching fraction of leptoquark decay to charged lepton, with $B_l = 1 - B$. Final states of decays of the leptoquark pair are $LQ\overline{LQ} \to lq\bar{l}\bar{q}$, $LQ\overline{LQ} \to lq\bar{\nu}\bar{q}(\bar{l}\bar{q}\nu q)$, and $LQ\overline{LQ} \to \nu q\bar{\nu}\bar{q}$ and have rates proportional to B_l^2, $2B_l(1 - B_l)$ and $(1 - B_l)^2$, respectively.

Table 2.1: Leptoquark states.

LQ Type	Fermion number	Charge	Coupling in 1^{st} generation
S_0^L	2	$-\frac{1}{3}$	$e_L u$ or νd
S_0^R	2	$-\frac{1}{3}$	$e_R u$
$\tilde{S}_0$	2	$-\frac{4}{3}$	$e_R d$
$S_{1/2}^L$	0	$-\frac{5}{3}$	$e_L \bar{u}$
		$-\frac{2}{3}$	$\nu \bar{u}$
$S_{1/2}^R$	0	$-\frac{5}{3}$	$e_R \bar{u}$
		$-\frac{2}{3}$	$e_R \bar{d}$
$\tilde{S}_{1/2}$	2	$-\frac{2}{3}$	$e_L \bar{d}$
		$+\frac{1}{3}$	$\nu \bar{d}$
S_1	2	$-\frac{4}{3}$	$e_L d$
		$-\frac{1}{3}$	$e_L u$ or νd
		$+\frac{2}{3}$	νd
V_0^L	0	$-\frac{2}{3}$	$e_L \bar{d}$ or $\nu \bar{u}$
V_0^R	0	$-\frac{2}{3}$	$e_R \bar{d}$
$\tilde{V}_0$	0	$-\frac{5}{3}$	$e_R \bar{u}$
$V_{1/2}^L$	2	$-\frac{4}{3}$	$e_L d$
		$-\frac{1}{3}$	νd
$V_{1/2}^R$	2	$-\frac{4}{3}$	$e_R d$
		$-\frac{1}{3}$	$e_R u$
$\tilde{V}_{1/2}$	2	$-\frac{1}{3}$	$e_L u$
		$+\frac{2}{3}$	νu
V_1	0	$-\frac{5}{3}$	$e_L \bar{u}$
		$-\frac{2}{3}$	$e_L \bar{d}$ or $\nu \bar{u}$
		$+\frac{1}{3}$	$\nu \bar{d}$

Table 2.2: Lower limits on masses of scalar leptoquark obtained in $p\bar{p}$ collisions for different branching fraction B_l for the decay to a charged lepton.

Generation	Lower mass limit	Channel	B_l
1^{st}	242 GeV	$p\bar{p} \rightarrow eqeq + X$	1
1^{st}	204 GeV	$p\bar{p} \rightarrow eq\nu q(eqeq, \nu q\nu q) + X$	1/2
1^{st}	98 GeV	$p\bar{p} \rightarrow \nu q\nu q + X$	0
2^{nd}	202 GeV	$p\bar{p} \rightarrow \mu q\mu q + X$	1
2^{nd}	180 GeV	$p\bar{p} \rightarrow \mu q\nu q(\mu q\mu q, \nu q\nu q) + X$	1/2
2^{nd}	123 GeV	$p\bar{p} \rightarrow \nu c\nu c + X$	0
2^{nd}	98 GeV	$p\bar{p} \rightarrow \nu q\nu q + X$	0
3^{rd}	99 GeV	$p\bar{p} \rightarrow \tau q\tau q + X$	1
3^{rd}	148 GeV (CDF)	$p\bar{p} \rightarrow \nu b\nu b + X$	0
3^{rd}	94 GeV (DØ)	$p\bar{p} \rightarrow \nu b\nu b + X$	0

CHAPTER 3
THE DØ DETECTOR AT THE FERMILAB ACCELERATOR COMPLEX

3.1 The Tevatron

The Tevatron collider complex accelerates proton and antiproton beams to an energy of 0.98 TeV each and collides them at two points where the main collider detectors, DØ and CDF, are located. During the Run I period of operation (1992-1996) the Tevatron supplied a center-of-mass energy of 1.8 TeV and about 130 pb^{-1} of total luminosity was delivered to each of the detectors.

In the period of time between the end of Run I and the beginning of Run II the Tevatron underwent a significant upgrade. The most important change was the substitution of the Main Ring with the Main Injector. That made available a large gain in the instantaneous luminosity. Also, the center-of-mass energy was increased to 1.96 TeV.

The Tevatron complex is a chain of different accelerators, Fig. 3.1. The particles obtain their final energy in the Tevatron Ring Synchrotron. To reach it, protons pass through the chain of accelerators:

- Cockroft-Walton preaccelerator
- Linear Accelerator

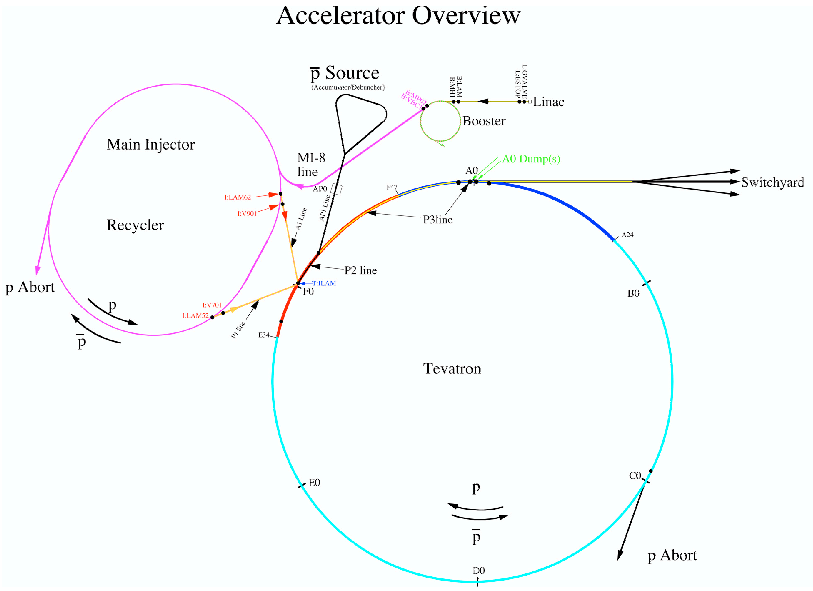

Figure 3.1: The Fermilab Collider Complex

- The Booster Synchrotron
- The Main Injector

The antiprotons created in the Anti-proton Source pass through the Debuncher and Accumulator before entering the Tevatron Ring Synchrotron.

3.2 DØ detector

3.2.1 The DØ Coordinate System

The DØ Cartesian coordinate system (Fig. 3.2) is defined such that the z axis points along the proton beam direction, the y axis points vertically upwards, and the x axis lies in the horizontal plane to correspond to a right-handed system. The

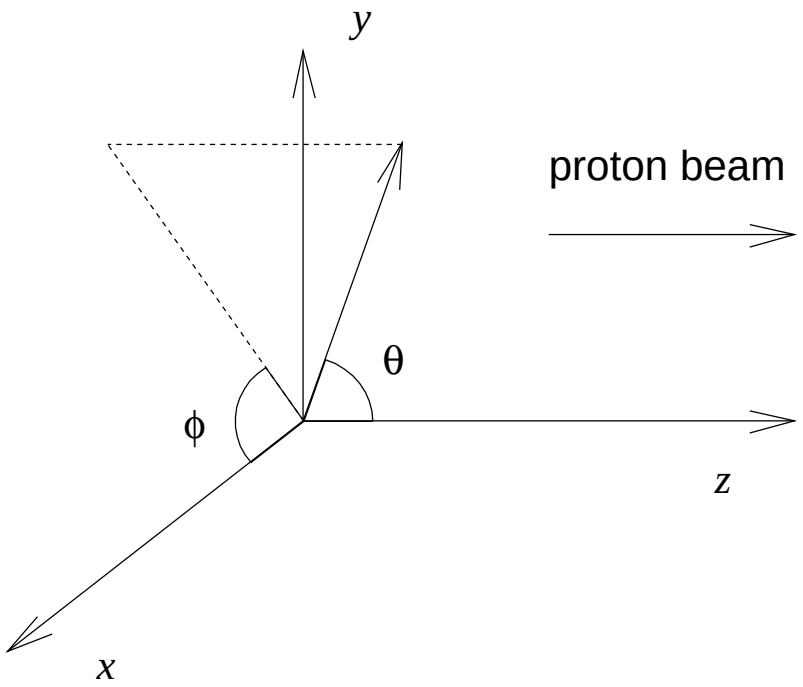

Figure 3.2: The DØ Detector Coordinate System.

azimuthal angle ϕ spans 0 to 2π. The polar angle θ is counted from the z axis, as usual.

A proton-antiproton collision results at the microscopic level in collisions of partons, which constitute each nucleon. Each parton carries some fraction of the total nucleon momentum. That fraction cannot be measured in a real high energy collider experiment because remnants of the collided nucleons are lost down

the beam pipe. Thus, the center-of-mass energy of the colliding partons remains unknown and the total momentum balance cannot be used for kinematical calculations. Nevertheless, the momenta are well balanced in the plane transverse to the beam direction. In the traditional set of variables which describe a particle's 4-momentum, (E, p_x, p_y, p_z), neither E nor p_z are invariant with respect to a boost along the z-direction.

The Lorentz transformation from the lab frame to the frame moving along the z-direction can be written as

$$p'_z = p_z \cosh y - E \sinh y$$
$$E' = -p_z \sinh y + E \cosh y$$

where y is rapidity.

An advantage of rapidity is that the boost along the z-direction just adds a constant. The rapidity can be expressed as

$$y = \frac{1}{2} \ln \frac{E + p_z}{E - p_z}$$

or

$$y = \frac{1}{2} \ln \frac{1 + \beta \cos\theta}{1 - \beta \cos\theta}$$

where $\beta = p/E$.

Using the rapidity, any particle with mass m can be described with a set of kinematic variables, (p_T, y, ϕ, m), in which the only variable that changes with a boost along the z-direction is the rapidity and changes by only an additive constant. In the limit $\beta \to 1$ we can define pseudorapidity as

$$\eta \equiv \frac{1}{2} \ln \frac{1 + \cos\theta}{1 - \cos\theta} = -\ln \tan \frac{\theta}{2}$$

which is a good approximation for Tevatron energies and is widely used. An angular

distance between two objects is often expressed in terms of $\Delta R = \sqrt{(\Delta\phi)^2 + (\Delta\eta)^2}$, where $|\Delta\phi| < 2\pi$.

The transverse momentum of a particle is defined in terms of the 3-momentum $\vec{p}$ as

$$p_T = |\vec{p}| \sin\theta.$$

The transverse energy by definition is

$$E_T^2 \equiv p_x^2 + p_y^2 + m^2 = p_T^2 + m^2 = E^2 - p_z^2$$

and will be equal to $E \sin\theta$ only in the limit $\beta \to 1$.

The invariant mass of two particles

$$M_{12}^2 \equiv (p_1^\mu + p_2^\mu)(p_{1\mu} + p_{2\mu})$$

in terms of the variables (p_T, y, ϕ, m) will be

$$M_{12}^2 = m_1^2 + m_2^2 + 2E_{T1}E_{T2}(\cosh\delta y - \beta_{T1}\beta_{T2}\cos\delta\phi),$$

where $\beta_T \equiv p_T/E_T = \beta\sin\theta$ and $\delta y \equiv y_1 - y_2$.

In the limit $\beta \to 1$

$$M_{12}^2 = 2E_{T1}E_{T2}(\cosh\delta\eta - \cos\delta\phi).$$

Particles that escape undetected create an imbalance in the measured total transverse momentum. This momentum imbalance is usually named (for historical reasons) as the missing energy, $\not\!\!E_T$. If a detector has a sufficiently large acceptance, only non-interacting particles will be undetected. In the case of the decay $W \to e\nu$, the missing energy is equal to the p_T of the neutrino. A knowledge of only the transverse component of the neutrino momentum is insufficient to reconstruct the mass of the W. However, one can calculate the transverse mass, which is invariant with respect to a boost along the z-direction,

$$M_T^2 \equiv (p_{T1}^\mu + p_{T2}^\mu)(p_{T1\mu} + p_{T2\mu}),$$

where $p_T^\mu = (E_T, \vec{\mathbf{p}}_T)$. In terms of the variables (p_T, y, ϕ, m) it can be written as

$$M_T^2 = m_1^2 + m_2^2 + 2E_{T1}E_{T2}(1 - \beta_{T1}\beta_{T2}\cos\delta\phi).$$

The transverse mass of the W decaying to the electron and neutrino can be written as

$$M_T^2 = 2E_T \not{E}_T (1 - \cos\delta\phi),$$

where E_T is the electron transverse energy, $\not{E}_T$ is used for the neutrino transverse energy and $\delta\phi$ is the angle between the azimuthal directions of the electron and $\not{E}_T$.

3.2.2 The Detector

The DØ detector [11] is a general-purpose particle detector designed to study proton-antiproton collisions at $\sqrt{s} = 2$ TeV at the Tevatron Collider. After successful operation in Run I, the detector was significantly upgraded before the start of the Run II physics program. Below we will describe the detector as it was operated in Run II.

The DØ detector (Fig. 3.3) has a nested structure, which is typical for most collider detectors. The major subsystems of the DØ detector are (from inner to outer radius):

- The Central Tracking System
- The Calorimeter
- The Muon System

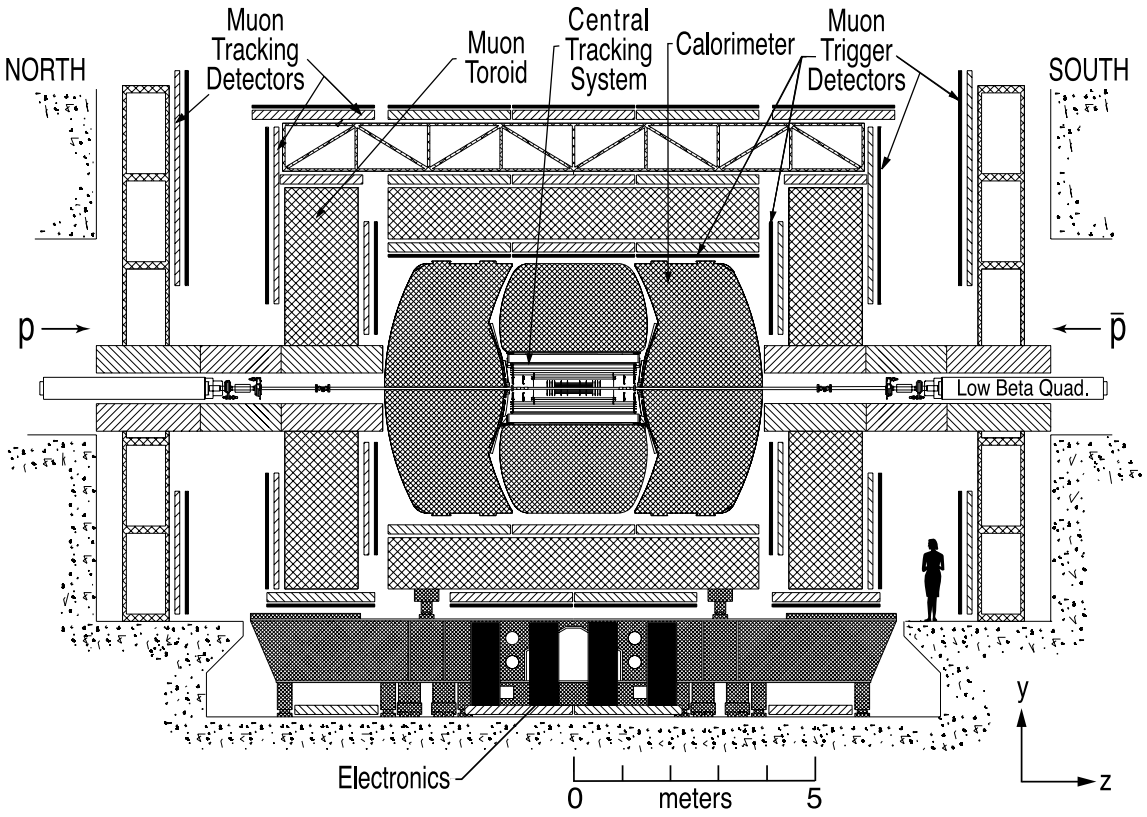

Figure 3.3: The DØ Detector

3.2.3 The Central Tracking System

In the inner layer, the beam crossing point is covered by the central detector. The central detector is embedded in a superconducting solenoid which operates with a magnetic field of 2 Tesla. The central detector is comprised of two independent subsystems:

- The Silicon Microstrip Tracker (SMT)
- The Central Fiber Tracker (CFT)

The Silicon Microstrip Tracker, Fig. 3.5, consists of six barrel detectors surrounding the beam line and 12 "F-disks" in the plane transverse to the beam direction. The barrels measure the $r - \phi$ coordinates. "F-disks" measure $r - z$ as well as $r - \phi$ coordinates. To provide coverage in pseudorapidity up to $|\eta| \leq 3$, the SMT has in the forward and backward regions two large diameter "H-disks." The SMT strip pitch of 50-80 μm provides a high spatial resolution to allow a precise reconstruction of the primary vertex and an accurate measurement of the distance of closest approach of the tracks.

The Central Fiber Tracker surrounds the SMT. It consists of layers of multiclad scintillating fibers covering the eight cylinders. The layers form doublets. Each cylinder bears one doublet of fibers oriented along the beam direction (axial layers) and one doublet of fibers alternating $\pm 3^\circ$ with respect to the beam direction (stereo layers).

The CFT data combined with the SMT measurements make possible track reconstruction and momentum measurement up to $|\eta| \leq 2.0$. The tracking possibilities of the upgraded DØ detector will be widely used in the current analysis for b-tagging as well as for the track confirmation of the calorimeter jets.

Scintillating fibers are attached to transport fibers that carry light to photodetectors. The photodetectors used are Visible Light Photon Counters (VLPC) operating at cryogenic temperatures. Fast timing characteristics of the scintillator readout make possible a Level 1 fast track trigger. The Central Tracker Trigger covers the pseudorapidity range $|\eta| \leq 1.6$.

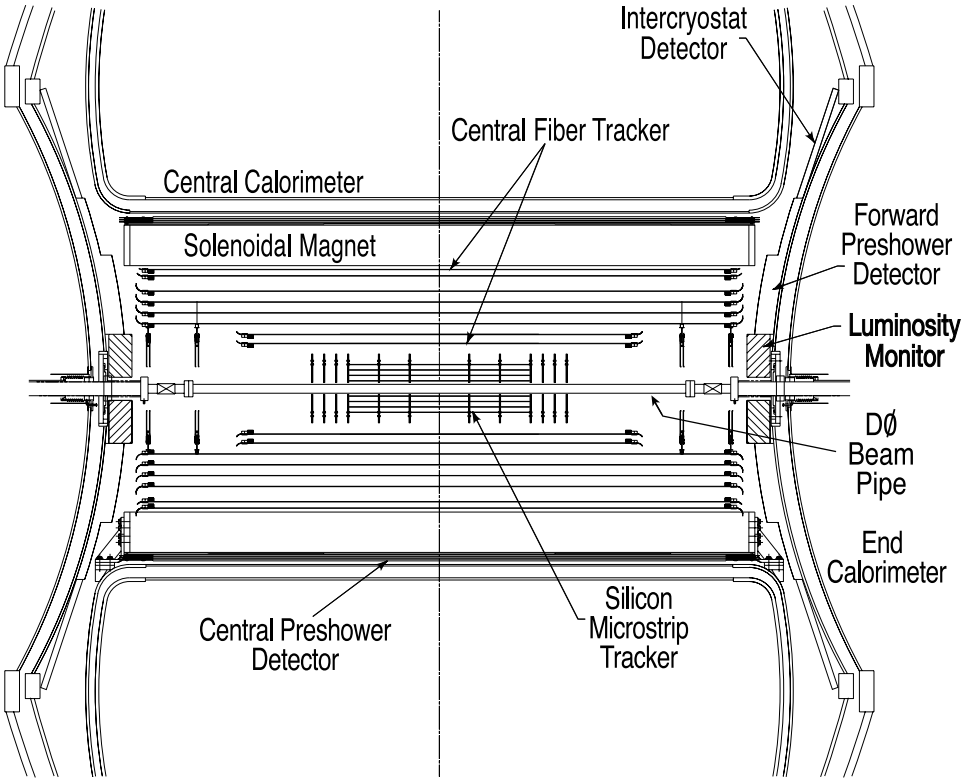

Figure 3.4: The DØ Central tracker

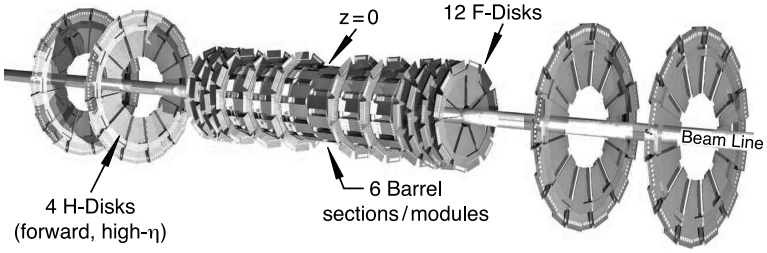

Figure 3.5: The DØ Silicon Microstrip Tracker

3.2.4 The Calorimeter

Due to the nature of the hard scattering processes, high energy collisions result in the formation of jets, which are sprays of secondary particles. To measure the

energy deposited in the form of jets, one needs to absorb these particles. This task is done by the Calorimeter System.

A perfect calorimeter system should be

- hermetic (cover a solid angle close to 4π)
- compact
- exhibit equal response to the particles of different types (ratio $e/h \approx 1$, where e stands for the response to electron and h to hadron)

The hermicity is needed for the reliable reconstruction of the energy of the particles that cannot be absorbed by the detector. The typical example is neutrino. The momentum information about such particles can be reconstructed (completely or in part) by calculating the total balance of the momenta for the event as measured by the hermetic calorimeter. Anything "missing" is presumed to be from neutral, non-interacting particles.

The compact design allows mounting an affordable muon system around the calorimeter. High-Z materials with short absorption length should be used to build a compact calorimeter. In addition, a compact calorimeter is less expensive.

Requiring $e/h \approx 1$ means that response of the calorimeter (i.e. magnitude of a signal generated by the calorimeter) to the hadron or the electron (photon) that entered it should be approximately equal. In fact, the hadrons deposit a significant fraction of their energy in the calorimeter in the form of electromagnetic energy (mainly through emission of η and π^0-mesons that decay electromagnetically like $\pi^0 \to \gamma\gamma$). This fraction has large fluctuations that affect the calorimeter resolution.

In addition, a large fraction of hadron energy escapes the measurement due to the production of particles which leave the calorimeter undetected (neutrons, neutrinos, muons) or the excitation or breaking up of the atomic nuclei.

The DØ calorimeter is a sampling calorimeter. It consists of inactive (absorber) and active components interlaced inside the detector. The main energy deposition occurs in the absorber by means of electromagnetic or hadronic showers. The second one, the active part, is used to measure a fraction of the energy that left the nearest layer of the absorber and is transformed into ionization or any other measurable form. Depleted uranium was chosen as an absorber for the calorimeter, while liquid argon (LAr) was selected as the active part. Depleted uranium as an absorber allows a compact and compensating calorimeter to be readily constructed. LAr as an active medium has the advantages of uniform gain, easy calibration, radiation hardness (stable parameters over time), and flexibility for segmentation.

The calorimeter consists of three main parts (Fig.3.6), each of which is, in fact, a separate calorimeter. They are the Central Calorimeter (CC) and two End Calorimeters (EC-North and EC-South). The Central Calorimeter covers the η region ± 1 while the End Calorimeters extend the total coverage to $|\eta| < 4.5$. To minimize any degradation of the transverse energy measurements, a boundary between the central and endcap calorimeters was chosen perpendicular to the beam axis. The calorimeter are divided into separate cells. The cells are arranged in towers with a pseudo-projective geometry (Fig. 3.7). To satisfy the pseudo-projective geometry, the centers of cells pertaining to the same tower are located along the tower axis projecting from the center of the detector while the cell walls are parallel

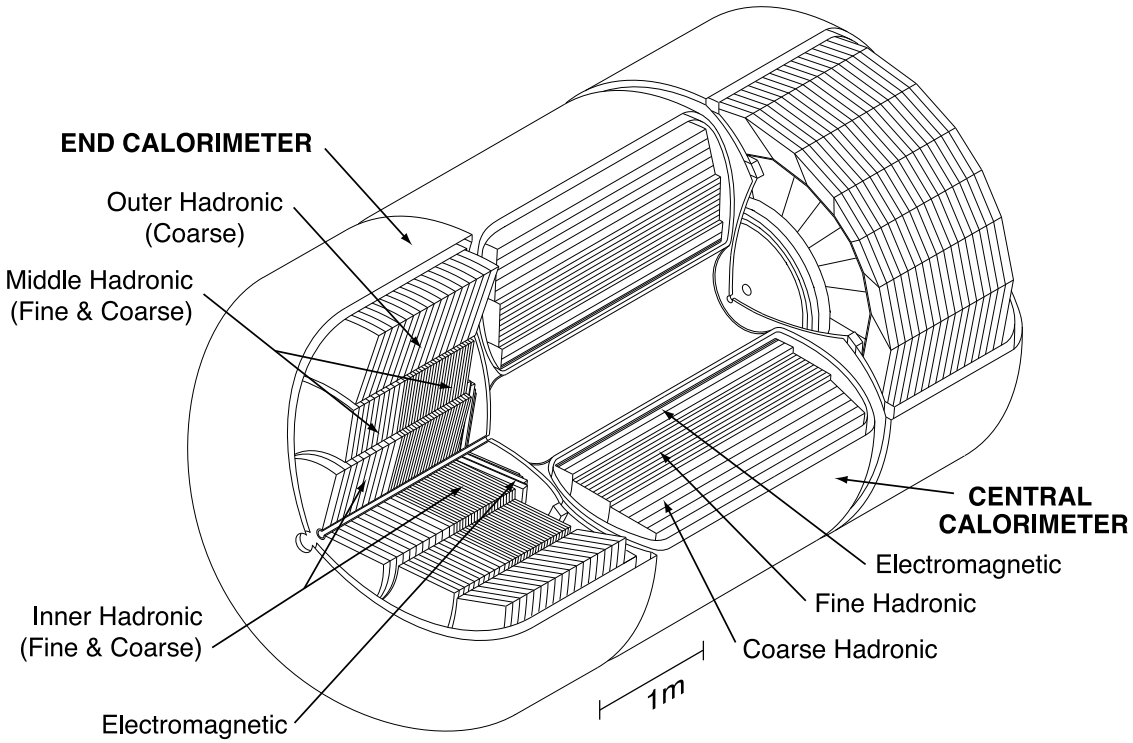

Figure 3.6: The DØ Calorimeter

or perpendicular to the absorber plates.

To provide good identification of electrons and photons as well as hadrons, the calorimeter was built using three types of modules:

- Electromagnetic (EM) modules use thin absorber plates from depleted uranium. The plate thickness is 3 mm in the CC and 4 mm in the EC.
- Fine Hadronic (FH) modules are built out of 6 mm plates of an alloy of 98.3% uranium and 1.7% niobium.
- Coarse Hadronic (CH) modules are made of thick 46.5 mm plates of copper

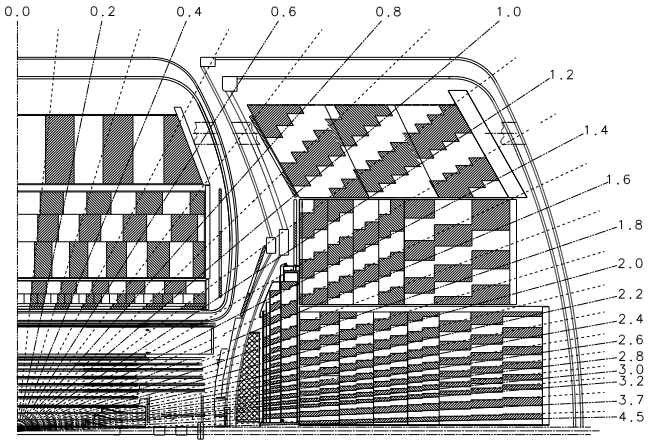

Figure 3.7: Pseudo-projective geometry of the DØ calorimeter

in the CC and stainless steel in the EC.

The structure of the unit cell is presented in Fig. 3.8. The charged particles from the shower create electron-ion pairs via ionization of the liquid argon in the 2.3 mm gap between the absorber plate and a G10 board. The electron-ion pairs are collected by the electrodes in the presence of an applied electric field. Metal absorbers serve as a ground electrode (cathode), and the readout boards are used as an anode. The high voltage applied to the readout boards ranges from 2.0 to 2.5 kV. The readout board consists of two sheets made of G10 material. A surface of each sheet is coated with an epoxy. The resistivity of the coated area is about 40 $M\Omega$. Several unit cells are combined into one readout cell. The electric signal from a readout cell is proportional to the energy deposited by the shower developed in the absorber plates of the unit cells.

As a result of the subdividing of the calorimeter in the central and endcap

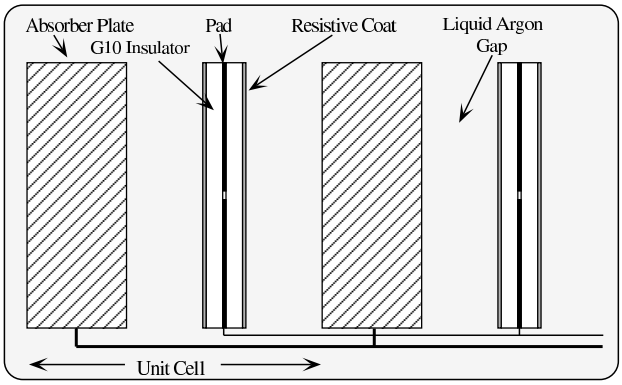

Figure 3.8: Calorimeter cell.

parts, the region $0.8 < |\eta| < 1.4$ is not well covered. To reduce the loss of performance, these regions were instrumented by detectors of two different types. One of them is the Massless Gap Detector (MGD). The Massless Gap Detector is located inside the Central Calorimeter. It consists of calorimeter cells containing only signal boards surrounded by liquid argon without the absorber plates. The segmentation of the MGD is the same as the rest of the calorimeter. The space between the central and endcap cryostats are filled by the Intercryostat Detector (ICD). The ICD consists of scintillator tiles arranged to match the pseudo-projective geometry of the calorimeter cells. The tiles are read by phototubes. The response across the

surface of a tile is uniform within 10%.

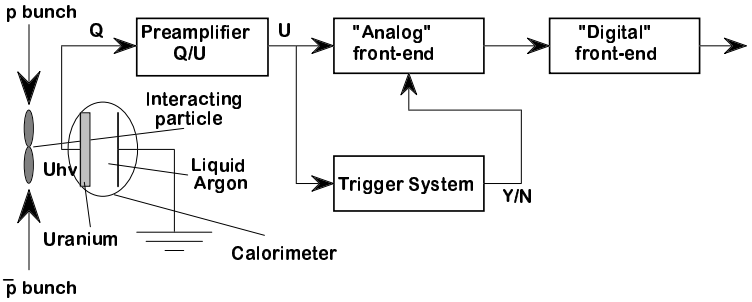

Figure 3.9: Simplified diagram of the calorimeter data flow path.

A schematic of the data flow path is shown in Fig. 3.9. Before the preamplifiers, special boards reorganize the signal from the module-structure scheme to the physical scheme in which the readout channels are arranged in the pseudo-projective $\eta - \phi$ towers. An important feature of the data flow is a splitting of each signal after the shaper. One path, the precision readout, leads to the baseline subtraction system (BLS). The BLS performs the signal sampling just before and after the beam crossing and takes the difference between the two. Another path carries the data to the Level 1 calorimeter trigger.

The calorimeter resolution is commonly written in the form (the sign $\oplus$ means sum in quadrature)

$$\sigma/E = \sigma_S/\sqrt{E} \oplus \sigma_N/E \oplus C$$

where

σ_S is statistical in its origin and corresponds to sampling fluctuations

σ_N corresponds to the noise contribution

C is a constant due to calibration errors

The parameters for the DØ calorimeter are listed in Table 3.1.

Table 3.1: Resolution Parameters for the DØ Calorimeter

	σ_S	σ_N	C
EM	0.13 $\text{GeV}^{1/2}$	0.40 GeV	0.015
HAD	0.80 $\text{GeV}^{1/2}$	1.5 GeV	0.04

The depth of each layer of the three calorimeter sections is shown in Table 3.2 in the units of *radiation length* X_0 and *absorption length* λ (for uranium $X_0 = 6$ cm and $\lambda = 199$ cm, so the electromagnetic section contains about 0.6λ).

Table 3.2: The depth of the calorimeter layers at normal incidence ($\theta = \pi/2$).

	EM	FH	CH
CC Depth	$2, 2, 7, 10\ X_0$	$1.3, 1.0, 0.9\lambda$	3.2λ
EC Depth	$0.3, 2.6, 7.9, 9.3\ X_0$	$1.2, 1.2, 1.2\lambda$	3.6λ

3.2.5 The Muon System

Due to their relatively high mass, muons lose energy mostly through ionization and not via bremsstrahlung at Tevatron energies. The lifetime of muons is large enough to appear as stable particles to the detector. As a result, muons created above about 3 - 5 GeV freely pass through the calorimeter. The same is true for muons from cosmic rays. Thus, deflection in a magnetic field is the only way to measure muon energy.

The DØ Muon System surrounds the calorimeter. It consists of magnetic toroids and three layers of detectors of three different types. In addition, the upgraded DØ detector allows improvement of the muon momentum measurement with the help of the tracking system (Fig. 3.3).

The toroids consists of five independent solid-iron toroid magnets with a magnetic field of approximately 1.8 T. The magnets cause the trajectories of the muons to bend in the $r - z$ plane. Due to the shape of the toroid, the magnetic field requires careful mapping to perform a proper measurement of the muon momentum. The accuracy of the momentum measurements using the toroid only is limited to $\sim 20\%$ by multiple scattering of the muons in the toroid material.

The layers of the muon system are named A, B, and C, from the inner to the outer part of the system. The magnetic system is divided into the central and two forward parts. Each layer consists of a plane of scintillators and either 4 planes of drift tubes in the A-layer (3 in the bottom part) or 3 planes in both B

and C layers (Fig. 3.10 - 3.11). The central part of the system uses Proportional Drift Tubes (PDT), while the forward parts use Mini Drift Tubes (MDT). The scintillator coverage is limited in some parts of the detector especially in the bottom of the innermost A-layer. The central muon system covers the pseudorapidity range $|\eta| < 1$. The forward muon system covers $1 < |\eta| < 2$.

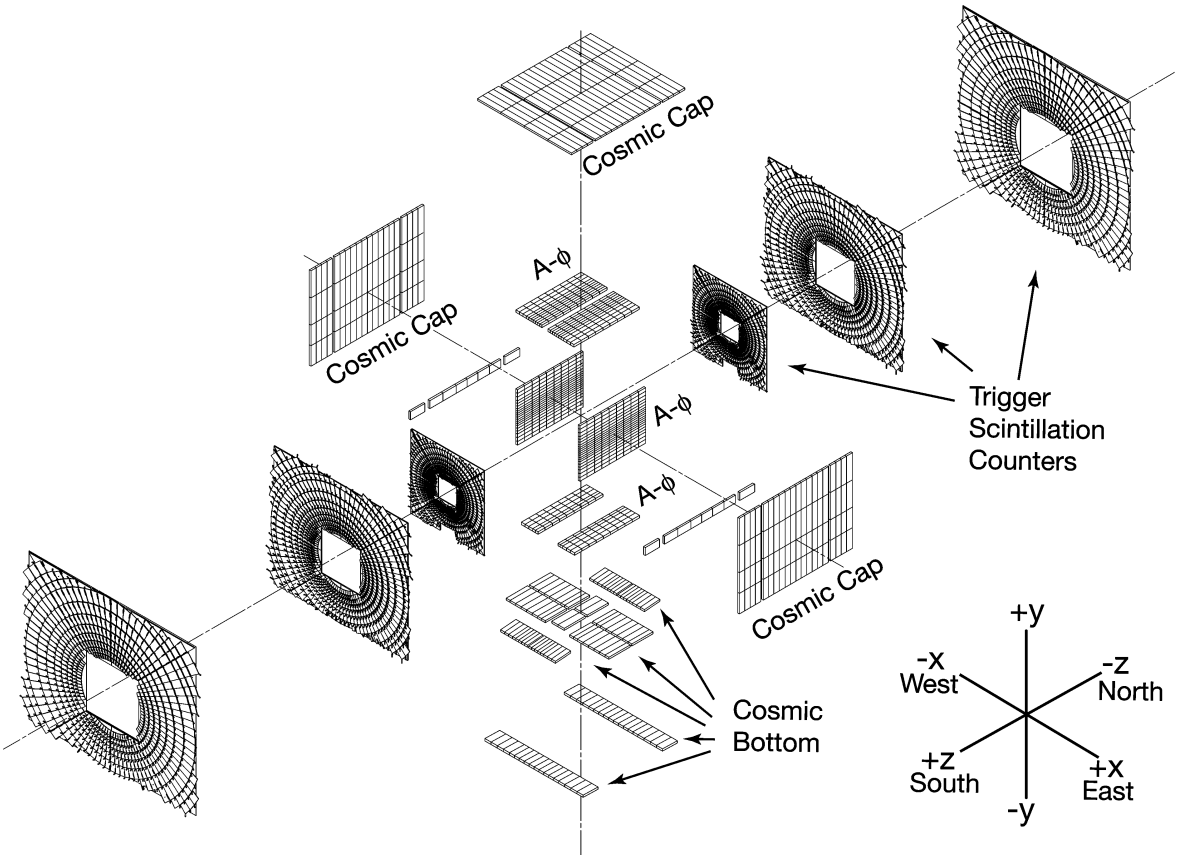

Figure 3.10: The DØ Muon System (Scintillators)

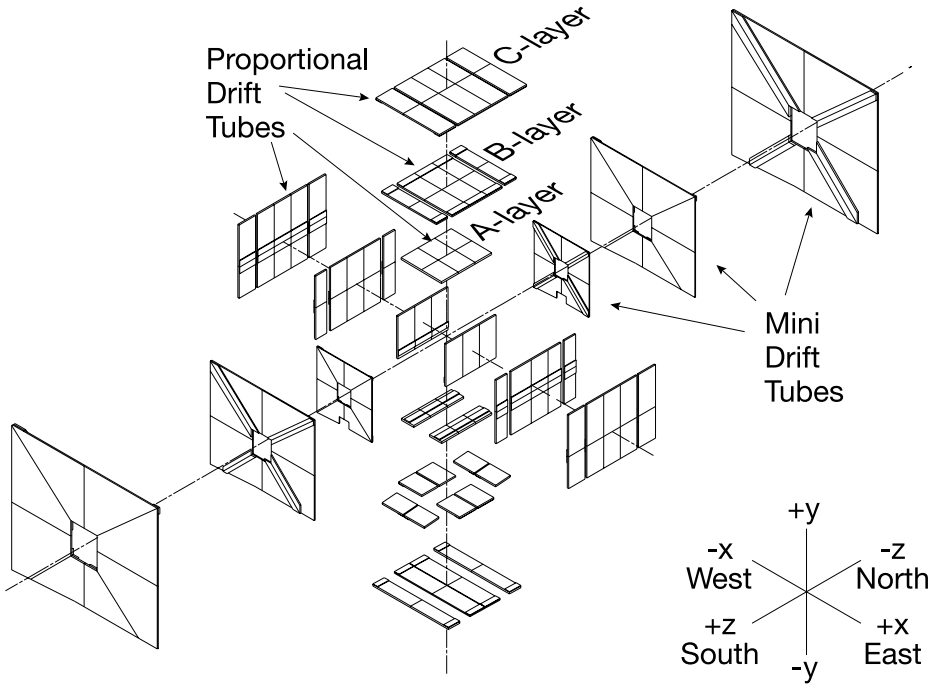

Figure 3.11: The DØ Muon System (PDT + MDT)

3.2.6 The DØ Trigger System

The $p\bar{p}$ beams overlap every 396 ns (this is called a bunch crossing); the corresponding rate is 2.5 MHz. A special electronic signal is generated just before the moment of the bunch crossing. This signal is needed for the detector electronics to start the current cycle of data acquisition. This signal corresponds to the firing of the zero bias trigger. An event triggered by the zero bias trigger is referred to as a zero bias event.

Most of the proton-antiproton collisions result in an elastic scattering of the incident nucleons or in low-p_T parton scattering events. The minimum bias event

occurs when the luminosity counters detect the products of the fragmentation. This event fires the minimum bias trigger. It is technically impossible and completely senseless to record the detector information about each minimum bias event. Since the ability of the recording system is limited to 50 events per second, the task of the trigger system is to select for recording only interesting events out of the minimum bias sample.

The DØ trigger system is comprised of three levels, Fig 3.12. Each level makes a decision if the event satisfies the criteria for an interesting event. In case of a positive decision, the event is transferred to the next trigger level. The decision is based on limited information due to the limited time available.

The most intense event stream floods Level 1. Due to severe time constraints the Level 1 trigger consists of hardware filters only, processed in parallel. It compiles a list of candidate events based on the fast information obtained from the

- calorimeter trigger towers (e.g., E_T above some threshold)
- muon scintillator counters (coincidence in time of pulses from the correspondent counters)
- CFT (e.g. hit pattern with a track momentum above some threshold)
- preshower detectors (e.g. energy deposition above some threshold)

The Level 2 trigger combines hardware decisions with fast software algorithms. At the preprocessor stage, a list of trigger objects is built using correlation algorithms and L1 detector-specific information. The global processor on the second

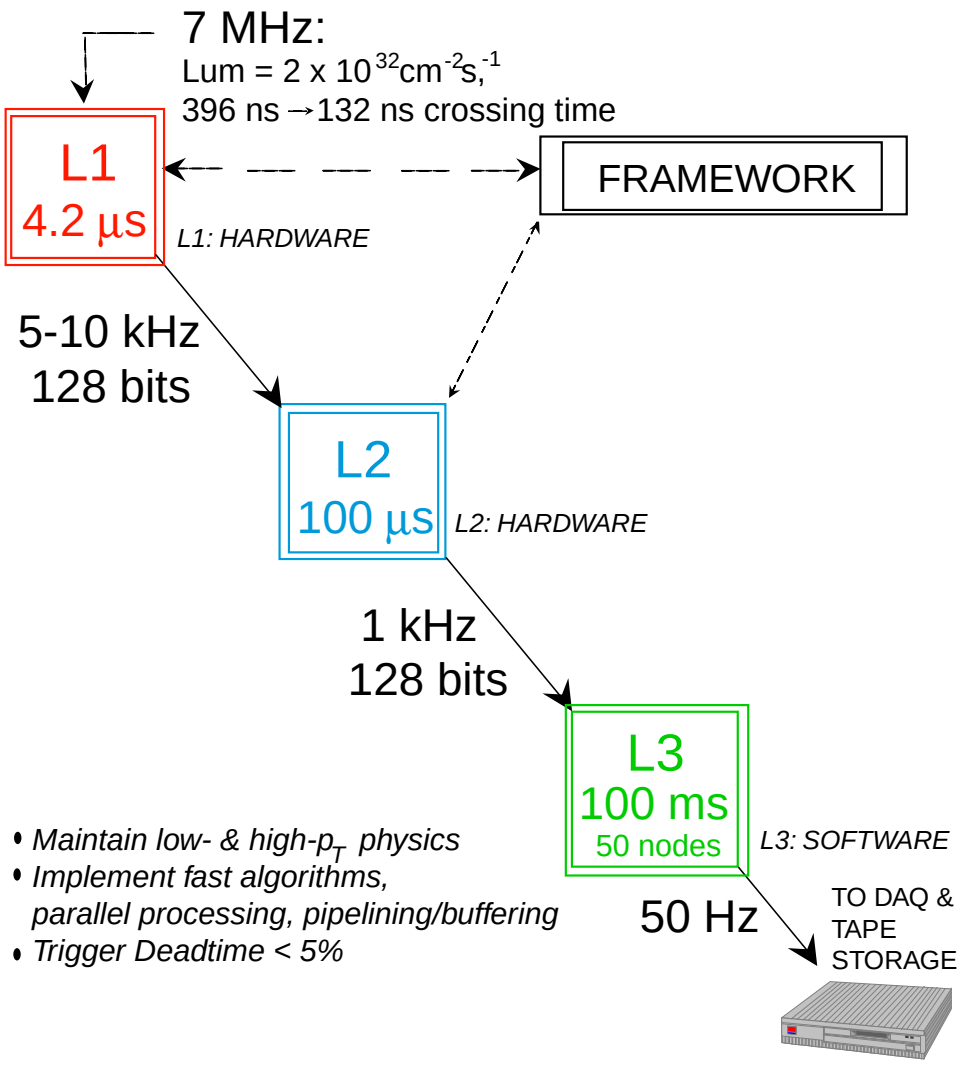

Figure 3.12: DØ trigger scheme layout and typical trigger rates. At the time of the actual taking of data used for the analysis the L1 rate was about 1800 Hz, the L2 rate was about 900 Hz.

stage gets this list via serial data highways on 128-bit data buses. The global processor compiles the correlations between the various detectors to form the trigger decision.

For example, the Level 2 muon trigger gets the Level 1 information about hits in the scintillators and in the drift chambers. Using 25 independent processors, it performs reconstruction of the muon tracks for different layers and regions of the detector in parallel [12]. Resulting segments of the muon track for the different sectors and layers are then passed to the other processors. The last combines muon segment information with timing and direction information.

The Level 3 and the data acquisition system (DAQ) are software-based. Moreover, the program codes used for the reconstruction of the physical objects do not differ from the corresponding programs used for the offline processing. This unification significantly simplified the maintenance of the Level 3 software. The code is run on a set of high-performance processors. After the full reconstruction of all physical objects, Level 3 runs the special filters corresponding to the list of triggers.

The work of the trigger system can be illustrated by the example of the calorimeter trigger MHT30_3CJT5 [13] used in the current analysis. An event will be triggered by MHT30_3CJT5 if it satisfies conditions specific to each trigger level. The Level 1 condition requires at least three calorimeter trigger towers with a transverse energy over 5 GeV. At a luminosity of $40 \cdot 10^{30}\ pb^{-1}$ it gave a rate of approximately 140 Hz. The Level 2 condition checks the missing transverse energy (MHT) built by the global Level 2 processor. The MHT is computed out of Level 2 jets with $E_T > 10$ GeV and constructed with 5×5 trigger towers. A cut

at 20 GeV on the MHT reduces the rate to 30 Hz. A corresponding MHT for the Level 3 is built out of Level 3 jets reconstructed using a simple cone algorithm. The Level 3 condition MHT $>$ 30 GeV decreases the final rate to approximately 2 Hz.

Some part of data in the analysis were collected with the JT1_ACO_MHT_HT trigger. Intended for higher instantaneous luminosity, it encompass the requirements of the MHT30_3CJT5 trigger plus additional requirements on acoplanarity (the azimuthal angle between the two leading jets) to be less than 168.75 and 170.0 degrees at levels 2 and 3, respectively and H_T (the scalar sum of jet E_T) to be over 50 GeV at level 3.

CHAPTER 4
EVENT RECONSTRUCTION

To perform an analysis of an event recorded by the detector, one needs to interpret the experimental information collected in terms of physical objects. Due to uncertainty pertaining to any measurement, this interpretation has a probabilistic character. This is valid with respect to the properties of the object (like energy) as well as with respect to the type of the object itself, keeping in mind the possibility of misidentification. Therefore generalized ID objects are used in an analysis instead of definite physical particles.

4.1 Track and Vertex Reconstruction

The kinematics properties of a reconstructed object depend on its emerging point to a large extent. A typical Tevatron event has only one hard scattering vertex. The presence of an additional primary vertex usually makes analysis of that event impossible.

The reconstruction of the primary vertex in the currently used algorithms requires a set of reconstructed tracks. Charged long-lived particles created in a hard proton-antiproton collision leave an ionization trace in the material of the central tracker and preshower. Muons that have enough energy also leave ionization traces in the calorimeter and in the outer muon system. The good spatial resolution of the central tracker makes it possible to reconstruct tracks using hits in the tracker

material. The 2 T magnetic field of the central solenoid magnet also plays an important role in the reconstruction.

There are a few track reconstruction algorithms implemented in DØ. The Road approach method used for the GTR tracking algorithm [14] will be described below. It uses the following:

- surface (cylinder or plane)
- path (a list of surfaces that the particle crosses)
- propagators (algorithms for propagating tracks from one surface to another)
- fitters (track-cluster matching algorithms)
- filters (track rejection algorithms)

The algorithm starts from the creation of "seed tracks." These seeds are propagated to the next surface. Hits found on this surface are fitted to create a new cluster of track hits. Clusters with a high value of χ^2 are rejected. Such selection creates a track candidate. The filters reject tracks failing certain criteria and leave the final set of tracks. The GTR algorithm starts from the outer part of the tracking system, from the CFT, and propagates tracks inside to the SMT.

Reconstructed tracks are used for the reconstruction of the vertices. The primary vertex is needed for reconstruction of jets, EM objects and missing E_T. However, the muon segments have been reconstructed in the muon system without using the primary vertex. Nevertheless, a knowledge of the primary vertex is important for the matching of reconstructed muons with the tracks.

The reconstruction of the primary vertex [15] starts from the selection of the tracks. This selection is performed in different categories:

- quality selection
- p_T cut
- cut on the distance of the closest approach to the beam axis

The selected tracks are fitted to a single vertex and the track with the maximum χ^2 is rejected. This procedure is repeated until the resulting χ^2 falls below a given value.

A similar procedure is used to determine if a secondary vertex is present in the event, which can be use to tag a b-decay.

4.2 Jet Reconstruction

A jet is a spray of particles that represents a propagation of the high energy parton after the complex processes of gluon radiation, showering and hadronization. Jet objects are usually connected with calorimeter activity. The signature of a jet is a large energy deposition in a compact group of the calorimeter towers. A jet is an object with its own 4-momentum, which, ideally, should correspond to the initial parton. The momentum of a jet is the sum of momenta of one-tower jets pertaining to the group. Each one-tower jet is considered as a massless particle emerging from the primary vertex. Thus, the determination of the correct primary vertex is vital for jet reconstruction.

The components of jet momentum are connected with transverse energy deposited in the i-th tower E_{Ti} and tower rapidity η_i as following:

$$p_x = \sum_{i=1}^{n} E_{Ti} \cos\phi_i$$
$$p_y = \sum_{i=1}^{n} E_{Ti} \sin\phi_i$$
$$p_z = \sum_{i=1}^{n} E_{Ti} \sinh\eta_i$$

The energy of a jet is the sum of the energies of its towers:

$$E = \sum_{i=1}^{n} E_i$$

To select calorimeter towers for the reconstruction of a given jet the *cone* algorithm is used. It starts from the selection of seeds towers with transverse energy over some threshold. A cone cluster of cells in (η, ϕ) space is created starting from each seed. Then the cluster with the highest E_T is considered as the preliminary jet. Cells within a cone R_{cone} will be added to the jet. After adding each cell the (η, ϕ) of the jet is recalculated using an iterative algorithm. Finally, if the transverse energy of the jet exceeds a threshold of 8 GeV, a jet is considered reconstructed. Some jets share the same calorimeter cells and a jets merging algorithm is used to avoid cell double counting. The momentum of jets is adjusted using the Jet Energy Scale corrections (JES) for such effects as pileup, out-of-cone showering, neutrino emission in semileptonic decay, etc. These corrections are determined by balancing the energies in 2-jet and photon-jet events.

4.3 Missing Energy Determination

The calorimeter missing energy is reconstructed similar to jets. Considering each calorimeter cell as a contribution of massless particle emerging from the primary vertex,

$$\not\!\!E_{Tx} = -\sum_{i=1}^{n} E_{Ti} \cos\phi_i$$
$$\not\!\!E_{Ty} = -\sum_{i=1}^{n} E_{Ti} \sin\phi_i$$

and

$$\not\!\!E_T = \sqrt{(\not\!\!E_{Tx})^2 + (\not\!\!E_{Ty})^2}$$

It is clear that "missing energy" really represents the missing transverse momentum. Choosing the correct primary vertex is required for the correct reconstruction of the missing energy. Before using the missing energy in analysis, it should be corrected for the contribution of muons, for JES corrections applied to jets, and for corrections to electromagnetic objects.

4.4 Transverse Energy and Missing Transverse Energy

The transverse energy (H_T) is the scalar sum of the transverse energies of all jets in the event:

$$H_T = \sum_{i=1}^{n} E_{Ti}$$

H_T represents the hadron activity in the event and is used as a powerful discriminator of physical processes involving decay of particles with high mass, like top quark.

While $\not\!\!E_T$ is opposite to the vector sum of the $\vec{E}_T$ of calorimeter cells, the

missing transverse energy ($\not\!\!H_T$) is built out of the $\vec{E}_T$ of reconstructed jets:

$$\not\!\!H_T = |\sum_{i=1}^{n} \vec{E}_{Ti}|$$

Determining $\not\!\!H_T$ is less time consuming than $\not\!\!E_T$ and is used in L2 and L3 for $\not\!\!H_T$-based triggers.

4.5 EM Object Reconstruction

The e/h ratio for the DØ calorimeter is close to 1. Therefore an electron and a hadron of the same energy produce the same calorimeter response. Nevertheless, electromagnetic and hadronic particles can be distinguished due to differences in shapes of electromagnetic and hadronic showers. An electromagnetic shower is much more narrow than a hadronic one and develops in the first (electromagnetic) layers of the calorimeter. The isolation of an EM object is defined as

$$iso = \frac{E_{tot}(0.4) - E_{EM}(0.2)}{E_{EM}(0.2)},$$

where $E_{tot}(0.4)$ is the total calorimeter energy deposited in the cone of 0.4 in $\eta - \phi$ space around the EM object and $E_{EM}(0.2)$ is the energy deposited in the cone of 0.2 in the electromagnetic layers only. This parameter is small for well identified electrons or photons, typically less than 0.15. For shower shape analysis a set of correlated variables such as energies deposited in each electromagnetic layers, total EM energy, vertex z-position, transverse shower width, etc. are used. A covariant matrix for observables x_i can be defined as follows:

$$M_{ij} = \frac{1}{N} \sum_{n=1}^{N} (x_i^n - \bar{x}_i)(x_j^n - \bar{x}_j),$$

where x_i is the value of observable i for particle n and $\bar{x}_i$ is the mean value of the observable for sample of N particles (initially found using a test beam data). Using

the inverse matrix $H = M^{-1}$ the likelihood parameter can be defined as

$$\chi^2 = \sum_{i,j}(x_i^n - \bar{x}_i)H^{ij}(x_j^n - \bar{x}_j)$$

Cuts on fraction of the electromagnetic energy, isolation and on the likelihood parameter helps to distinguish electromagnetic and hadron objects. Electrons can be separated from photons by requiring a track.

4.6 Muon Reconstruction

The reconstruction of a muon track starts from separate reconstruction of segments in layer A and in layers B and C of the muon detector. On the next step the A- and BC-segments are matched using an algorithm which propagates the muon track through the magnetic field of the toroid. Thus a muon momentum in the local muon system will be obtained. To improve the momentum resolution a muon track is matched with tracks of the central detector. If that global fit converges, the momentum of the central track is used for the muon. The momentum resolution achieved with the global fit is equal to the momentum resolution of the central tracker ($\Delta p/p = 0.02 \oplus 0.002 p_T/\text{GeV}$), which is far better than resolution of the local muon system ($\Delta p/p = 0.18 \oplus 0.003 p_T/\text{GeV}$).

Reconstructed muons are processed by an analysis package that uses muon parameters to match muon track with the track in the central detector, supplies information about muon isolation and quality, and defines some additional parameters. With respect to quality it classifies muons as *loose*, *medium* or *tight*. The muon quality is based on the number of fired elements of the muon system (including scintillator hits) and fit quality. *Tight* muons have chamber and scintillation

hits in A, B and C layers, converged fit of A and BC segments and a matched track in the central detector. *Medium* and *loose* muons have less strict requirements. This analysis mostly uses *medium* muons. This includes essentially all muons with A and BC segments. It also includes those A- or BC-only segments which match a central track and are located in the bottom of the detector. The reconstruction efficiency for *medium* muon was measured in the data to be about 83%.

CHAPTER 5
SEARCH FOR THIRD GENERATION SCALAR LEPTOQUARKS

The search for the pair production of third generation scalar leptoquarks was performed in data collected by the DØ detector from March 2002 to November 2004. The data correspond to an effective integrated luminosity of 310 pb^{-1}.

5.1 Signal and Background

5.1.1 Signal Features

The signature of the $LQ\overline{LQ} \rightarrow b\bar{b}\nu\bar{\nu}$ decay is two energetic b-jets accompanied by significant $\not\!\!E_T$. After the two b-jets candidates are selected using b-tag methods, the fraction of their transverse energy becomes a powerful discriminating factor (introduced in [17]). We denote

$$X_{jj} \equiv (E_{Tjet1} + E_{Tjet1})/(\Sigma_{jets} E_T)$$

where E_{Tjet1} and E_{Tjet2} are the transverse energies of the two tagged jets (in case of the μ-associated jets, the $\Sigma_{muons} P_T$ is added to the numerator and denominator).

Figures 5.1-5.6 show distributions of $\not\!\!E_T$ and E_T of leading jets for a simulated decay of a leptoquark pair with $M_{LQ} = 150$ GeV. Fig. 5.7 shows the p_T of reconstructed muons coming from the decay of b or c quarks. Some leptoquark events have more than one muon arising from semileptonic decays. Fig. 5.8 gives the p_T distribution of reconstructed muons for the dimuon channel.

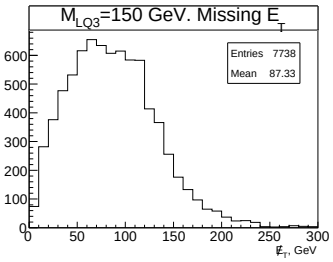

Figure 5.1: Missing E_T. M_{LQ3}=150 GeV for all Figs. 5.1-5.8

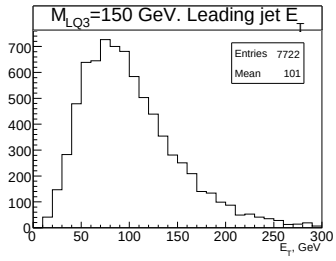

Figure 5.2: E_T, first leading jet.

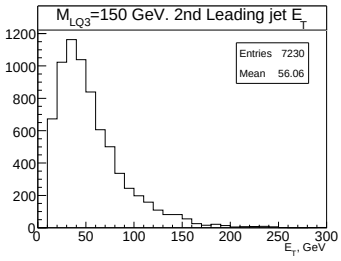

Figure 5.3: E_T, second leading jet.

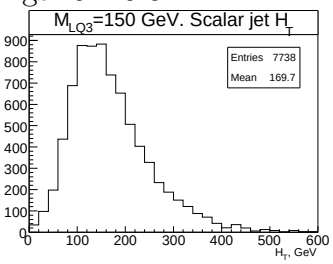

Figure 5.4: Scalar jet H_T.

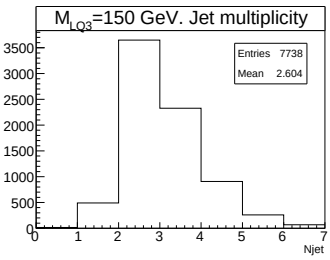

Figure 5.5: The number of jets $E_T > 20$ GeV.

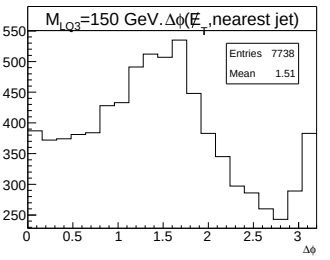

Figure 5.6: $\Delta\phi(\not{E}_T$,jet)

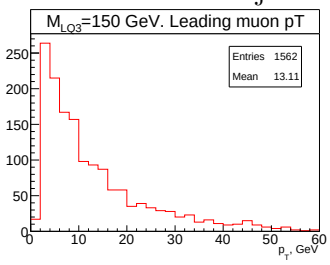

Figure 5.7: p_T of the leading muon from semileptonic decay.

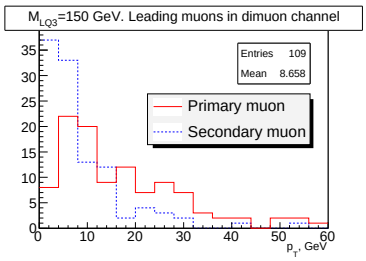

Figure 5.8: p_T of muons in the dimuon channel.

The signal samples (Table 5.1) for leptoquark masses 150 - 220 GeV were generated with PYTHIA [18]. The parton density functions used were CTEQ5L [19]. An average of 0.8 minimum bias events were superimposed.

Table 5.1: Generated signal samples

M_{LQ3}, GeV	σ(NLO), pb	Events generated	CSG request ID
150	1.59	7750	12554
160	1.08	10750	15183
170	0.75	10250	15184
200	0.27	7500	15184 input parameters, $M_{LQ3} = 200$
220	0.14	6500	15184 input parameters, $M_{LQ3} = 220$

5.1.2 Background

The instrumental background to our signal comes mostly from QCD processes with fake $\not\!\!E_T$ due to jet mismeasurement or calorimeter noise. The background dominates the low $\not\!\!E_T$ region. A different type of instrumental background comes from physical processes involving leptonic decay of W boson, when a lepton remains unreconstructed or is misidentified as a part of a hadronic jet.

Physical backgrounds include processes with real $\not\!\!E_T$. The most important of them are leptonic decays of W/Z bosons + jets events and processes with a top quark. To estimate the contribution of the Standard Model processes we used the official Monte Carlo samples listed in Table 5.2. The "jj" in a sample's name

means that the sample was generated with light (u, d, s) quarks in the initial state, while "$b\bar{b}$" indicates the only b-quarks were generated in the initial state. Thus, no overlaps between the samples on the generator level are present. For all samples except $t\bar{t}$ and single top, the NLO cross-section were obtained from [20]. Cross sections for $t\bar{t}$ production were taken from [21] and single top production from [22]. At the parton level the single top MC was generated with COMPHEP [23], while ALPGEN [24] was used for all other samples. These events were then processed with PYTHIA [18], which performed simulation of initial and final state radiation and of jet hadronization. CTEQ5L [19] was used as a parton density function in all cases. A Poisson-average of 0.8 minimum bias events was overlaid on each simulated event. An additional smearing of jets, muons and EM-objects was performed to reproduce the resolution observed in data.

Combining the currently available ALPGEN+PYTHIA samples generated for different jet multiplicities requires a special procedure to match partons with particle jets to avoid double counting of configurations [25]. The existing code performs this procedure in a very inefficient way; e.g. only about 5% of events survived selection for some samples. As a result the statistical error becomes unacceptably large. We are using ALPGEN samples with two jets in the final state, according to the jet topology of this analysis. The validity of this approach and introduced systematic errors are discussed in Appendix B. The Monte Carlo events were reconstructed in the same fashion as experimental data.

Table 5.2: MC samples used for background processes

Process	σ(NLO), pb	Events generated
W($\mu\nu$)+ jj	287.6	266412
W($e\nu$)+ jj	287.6	188967
W($\tau\nu$)+ jj	287.6	27996
Z($\nu\nu$)+ jj	174.0	80986
W($\mu\nu$) + $b\bar{b}$	4.16	98951
W($e\nu$) + $b\bar{b}$	4.16	97950
W($\tau\nu$) + $b\bar{b}$	4.16	27249
Z($\nu\nu$) + $b\bar{b}$	1.73	29239
$t\bar{t} \rightarrow b\bar{b}l\nu l\nu$	0.688	9000
$t\bar{t} \rightarrow b\bar{b}l\nu jj$	2.92	44248
$t\bar{t} \rightarrow b\bar{b}jjjj$	3.09	57250
Single top, $\mu\nu bq\bar{b}$	0.259	15500
Single top, $\mu\nu b\bar{b}$	0.115	30500

5.2 Data Sample

We worked with data collected by the DØ detector between May 2002 and November 2004. The $\not\!\!H_T$-based triggers were used to select events. Runs used were not qualified bad for calorimeter, muon and CFT subsystems. The triggers required the presence at least three calorimeter trigger towers with transverse energy

over 5 GeV at Level 1 and $\not\!\!H_T$ over 20 GeV and 30 GeV at Level 2 and Level 3, respectively. Part of the data was collected with the requirement that the azimuthal angle between the two leading jets be less than 168.75 degrees at Level 2 and less than 170 degrees at Level 3. Also $H_T > 50$ GeV was required at Level 3. Detailed description of the trigger can be found in Appendix A.2. The resulting subsample defined here as "MHT" corresponds to an effective luminosity of 310 pb^{-1}.

5.2.1 Parameterization of triggers for SM samples

A trigger parameterization [13] was used for the simulated samples. The parameterization was obtained using multijet events which fired muon triggers. The resulting trigger efficiencies for the signal sample of $M_{LQ3} = 150$ GeV vs $\not\!\!E_T$, $\not\!\!H_T$ and the leading jet E_T are plotted in Figs.5.9-5.14. The trigger becomes 90% efficient at about $\not\!\!E_T = 60$ GeV or $\not\!\!H_T = 55$ GeV. The overall trigger efficiency for LQ3 signal depends on leptoquark mass and ranges from 70% for $M_{LQ} = 150$ GeV to 85% for $M_{LQ} = 220$ GeV.

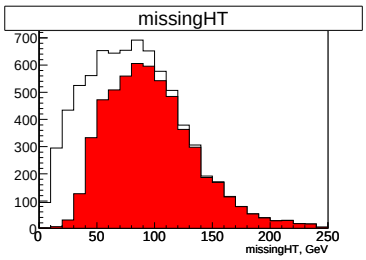

Figure 5.9: Signal $\not\!\!H_T$ for all events (open) and for passed trigger (colored).

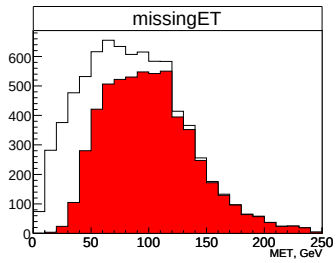

Figure 5.10: Signal. $\not\!\!E_T$ for all events (open) and for passed trigger (colored).

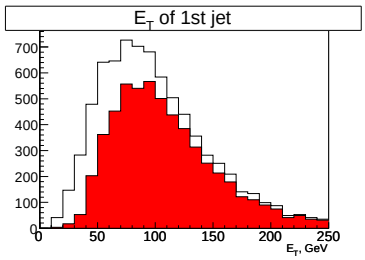

Figure 5.11: Signal. E_{Tjet1} for for all events (open) and for passed trigger (colored).

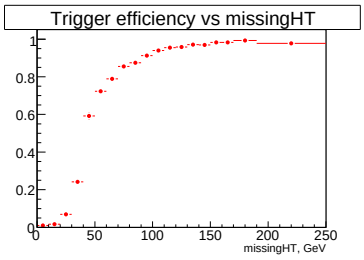

Figure 5.12: Differential trigger efficiency vs $\not\!\!H_T$.

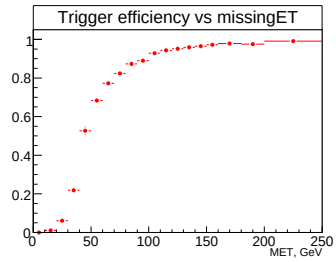

Figure 5.13: Differential trigger efficiency vs $\not\!\!E_T$.

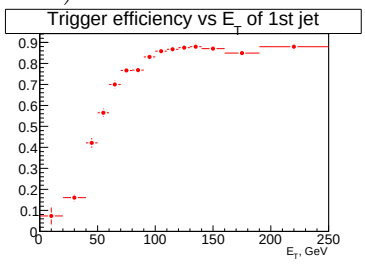

Figure 5.14: Differential trigger efficiency vs E_{Tjet1}.

5.3 Definition of objects

"Good" physical objects such as jets, muons and EM-objects in data and MC events were filtered out of all reconstructed objects using quality criteria which are standard for all DØ analyses. If not mentioned separately the objects indexes (like jet_1, ... ,jet_x) correspond to the value of E_T in decreasing order.

5.3.1 Jets

In this analysis we are using jets reconstructed by the simple cone algorithm with radius 0.5. The jet energy scale corrections were applied to all "good" jets.

"Good" jets are defined as having:

- fraction of energy deposited in the electromagnetic calorimeter layers between 0.05 and 0.95
- fraction of energy deposited in the coarse hadronic calorimeter layers < 0.4
- confirmed by L1 trigger towers
- no reconstructed EM objects with p_T over 5 GeV in $\Delta R < 0.4$

These "good" jets are subject to the Jet Energy Scale (JES) corrections. The resulting JES corrections were also used for correcting $\not\!\!E_T$.

Jets that failed the "good" jet criteria are believed to be a byproduct of calorimeter noise or a misidentified EM object. The presence of such "bad" jets with significant E_T in the event makes the $\not\!\!E_T$ of the event undetermined.

5.3.2 Muons

For leptoquark analysis we used muons of *medium* quality. For parts of the analysis which deal with $W \rightarrow \mu\nu$ we also used *loose* muons with the requirement to have hits in the B and/or C layers and a matched central track. For data events we used the p_T value corrected by the muon analysis package. Momenta of MC muons were additionally smeared to satisfy the experimental data.

The current analysis uses the muons produced in semileptonic decays of b quarks or in the chain decay $b \rightarrow c \rightarrow \mu$ to tag b-jets. We associate a muon with a jet if a cone in pseudorapidity- and azimuthal-space, $\Delta R = \sqrt{(\Delta\eta)^2 + (\Delta\phi)^2} < 0.5$, where η is pseudorapidity and ϕ is azimuthal angle. We applied a veto on events with any isolated *medium* muons with $p_T > 5$ GeV or *loose* muons with $p_T > 10$ GeV in order to reduce $W \rightarrow \mu\nu + jets$ events.

5.3.3 EM objects

We do not put any additional requirements on EM objects over the standard definition. An event is vetoed if it contains an isolated EM object with p_T over 5 GeV in order to reduce $W \rightarrow e\nu + jets$ events.

5.3.4 Missing E_T

The $\not\!\!E_T$ used is modified by JES corrections to jets. We then redo the muon corrections in data using the corrected value of muon p_T. In addition to *medium* muons, $\not\!\!E_T$ is corrected for the selected *loose* muons both in data and in MC.

5.4 Data cleaning

5.4.1 Primary vertex

Events without a reconstructed primary vertex were rejected at the preselection stage. For the effective usage of jet track confirmation, the primary vertex is required to be ±60 cm from the center of the detector.

5.4.2 Bad jets

Events with high $\not\!\!E_T$ include a large percentage of regular QCD events with mismeasured jets and therefore fake $\not\!\!E_T$. Therefore we rejected events containing bad jets with $E_T > 15$ GeV.

5.4.3 Track confirmation

We used a track confirmation algorithm for the confirmation of any good jet with $E_T > 15$ GeV and $|\eta_{det}| < 1.5$. That detector η range corresponds to the fiducial region of the central detector. A jet is considered confirmed if the scalar sum of the p_T of tracks associated with it exceeds 5% of the jet E_T. The tracks used should have at least 8 CFT hits. The distance of closest approach to the primary vertex should not exceed 2 cm in r and 5 cm in z.

The effect of the data cleaning cuts is illustrated in Fig. 5.15. It demonstrates the changing of the $\not\!\!E_T$ distribution of preselected events after removing bad jets with $E_T > 15$ GeV and requiring track confirmation for any jet with $E_T > 15$ GeV and $|\eta_{det}| < 1.5$. To emphasize the effect of track confirmation we applied it to

selected events ($\not\!\!E_T > 40$ GeV and $\Delta\phi > 0.5$ between direction of $\not\!\!E_T$ and nearest jet over 15 GeV) plus the requirement that the primary vertex be within ± 60 cm from the center of the detector, and then took events with the leading jet in the $|\eta_{det}| < 1.5$ region. The blue histogram shows preselected events; the yellow shows the effect of removing bad jets, and the red histogram is the cleaned sample after additionally requiring track confirmation.

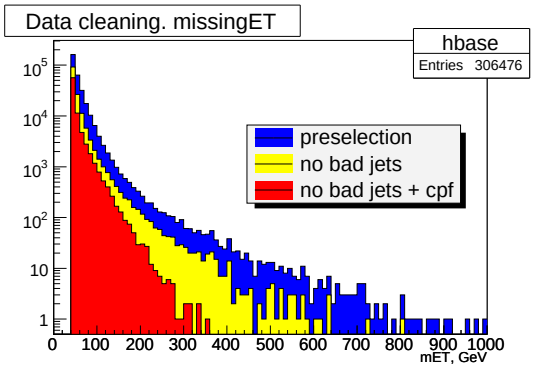

Figure 5.15: Bad jets and jet track confirmation

5.4.4 Cleaning inefficiencies

We studied the inefficiency introduced by cleaning on a signal with natural $\not\!\!E_T$ using $W \rightarrow \mu\nu + jets$. This process was chosen because its features are similar to the leptoquark signal. It is also one of the most important backgrounds and can be selected relatively easily with the desired purity.

We selected 1097 $W \rightarrow \mu\nu$ events directly from the data sample. The following criteria were used:

- $\not\!\!E_T > 20$ GeV
- $E_{Tjet1} > 40$ GeV, $E_{Tjet2} > 20$ GeV
- isolated muon, no other isolated muons or electrons with $p_T > 5$ GeV
- $\Delta\phi$ between the muon and $\not\!\!E_T$ is required to be greater than 0.6
- reconstructed W transverse mass should be below 200 GeV

Fig. 5.16 presents the W transverse mass and Fig. 5.17 shows $\not\!\!E_T$. The red histogram represents our set of SM processes while the blue histogram shows the contribution of the $W \to \mu\nu + 2\ jets$ separately. Other processes contribute about 10% in total. The simulated samples include the difference in track-matching and isolation efficiency between data and MC. To find the inefficiencies of the bad jet removing and the jet track confirmation we selected the central part of the m_T distributions (50 - 90 GeV). The results are summarized in Table 5.3. The Data/MC ratio was applied to all Monte Carlo samples.

Table 5.3: The efficiencies due to cleaning cuts for data and Monte Carlo.

	Data	MC	Data/MC ratio
track conf., first leading jet	0.972 ± 0.007	0.997 ± 0.001	0.975 ± 0.007
track conf., first two leading jets	0.954 ± 0.010	0.993 ± 0.002	0.961 ± 0.010
"bad jet" removing	0.972 ± 0.007	0.986 ± 0.003	0.985 ± 0.008

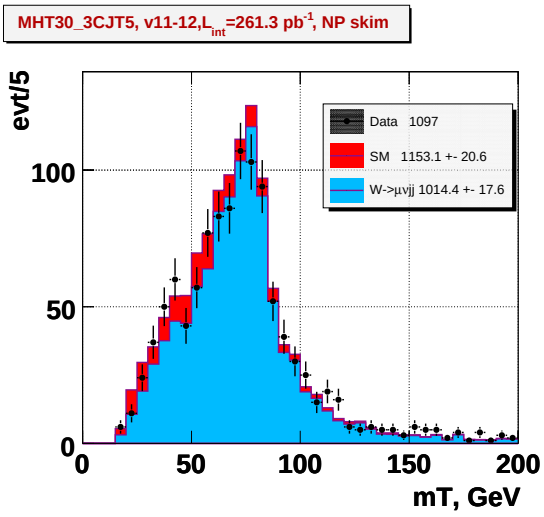

Figure 5.16: W transverse mass for the $W \to \mu\nu$ subsample.

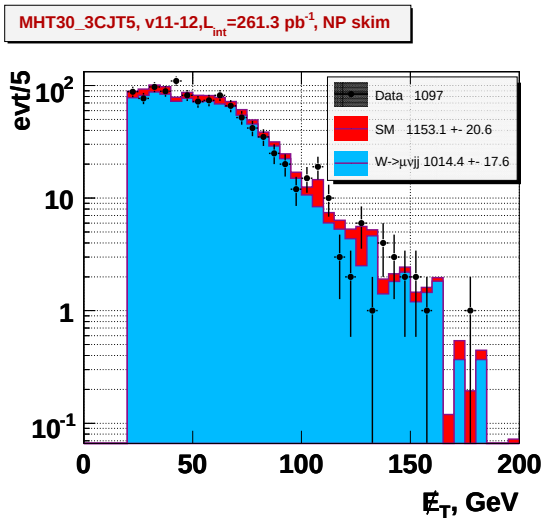

Figure 5.17: $\not\!\!E_T$ for the $W \to \mu\nu$ subsample.

5.5 The Impact Parameter Tagging Analysis

5.5.1 Preselection

The two b-jets in LQ events can be tagged by using either the vertex detector or by the presence of a muon. This section describes the first, the muon tagging is discussed in the next section, and the final results will use both methods. In preparation for vertex tagging a "pretag" sample was constructed with the following cuts (Table 5.4).

To clean the sample from the instrumental background, events with a bad jet with $E_T > 15$ GeV were removed, and all jets with $E_T > 15$ GeV and $|\eta_{det}| < 1.5$ were required to be track-confirmed (section 5.4.3). The leading jet has to have $|\eta_{det}| < 1.5$ to pass the track confirmation criteria. The azimuthal angle between the direction of $\not\!\!E_T$ and the nearest jet with $E_T > 15$ GeV was required to be over 0.7. This removes events where the energy of one jet was undermeasured.

To stay away from the trigger inefficiencies we required $\not\!\!H_T > 40$ GeV and the first leading jet $E_T > 40$ GeV. Requiring the acoplanarity (the azimuthal angle between the two leading jets) < 165 degrees allowed us to process the data collected with all triggers used in the same fashion.

We also required $\not\!\!E_T > 70$ GeV, which removes a significant part of the Standard Model background without much loss in signal acceptance.

Following our study of the validity of using of 2-jet ALPGEN Monte Carlo samples for the description of real data (Appendix B) we require the second leading

jet E_T to be over 20 GeV.

LQ signal does not produce isolated leptons. Therefore we applied a veto on events with isolated muons ($p_T > 5$ GeV if *medium* or > 10 GeV if *loose*) or EM objects ($p_T > 5$ GeV). This cut removes events with reconstructed isolated leptons originated from W/Z+jets processes.

The pretag cuts for the Impact Parameter Tagging Analysis also included

- $\Delta\phi(\not\!\!E_T$, the first leading jet) < 3.0 (instrumental background suppression)
- $H_T > 110$ GeV to suppress the SM background
- isolated track veto

The last cut on isolated track removes a fraction of W/Z+jets events in which a lepton remained unreconstructed. The track is considered as isolated if a hollow cone with radii 0.05 and 0.2 around it does not contain tracks with $p_T > 1.5$ GeV. Because up to 40% of signal events contain such isolated tracks inside a jet, we also put a combined restriction on the track ΔR (angular distance of the isolated track from the nearest jet) and on the track p_T. High-p_T products of heavy quark decay tend to be close to jets axis, while leptons originated from W decay randomly associated with jets are distributed uniformly in ΔR. Therefore, we discard only events which contain a leading isolated track with $\Delta R \times p_T > 3.5$ GeV. The cut value is illustrated in Fig. 5.18. Fig. 5.19 shows the transverse mass of the leading isolated track in the discarded events. A similar cut on $\Delta R \times p_T$ for muons is used in the muon analysis described below. Due to good agreement between the data

and MC before and after the cut, no correction factor on data/MC efficiencies was applied.

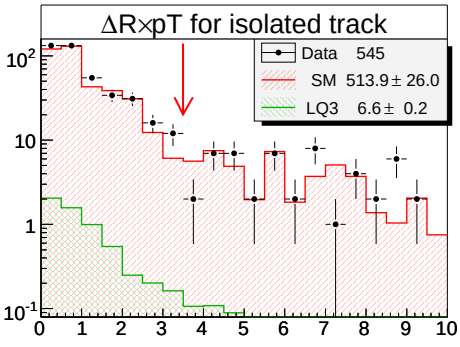

Figure 5.18: Product $\Delta R \times p_T$ for the leading isolated track.

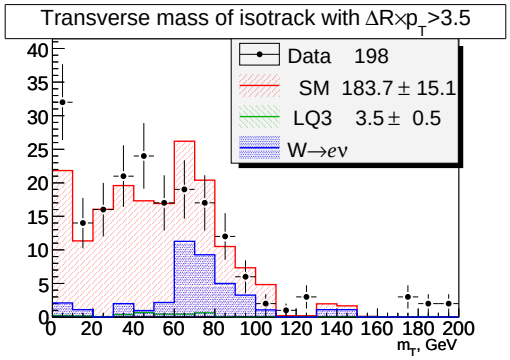

Figure 5.19: The transverse mass of the leading isolated track with $\Delta R \times p_T > 3.5$.

The cuts flow is summarized in Table 5.4.

Figs. 5.20-5.25 show distributions of $\not\!\!E_T$, scalar jets H_T, jets E_T and jet multiplicity for collider data and the simulation of the signal and the Standard Model background. Some excess of data over Monte Carlo in the first bins of the $\not\!\!E_T$ distribution can be attributed to instrumental effects. For instance, on Fig. 5.26 (which represents the ϕ of the $\not\!\!E_T$) a clear excess of data can be seen on the side part of the detector. Nevertheless, this data sample overall contains very little instrumental background and reproduces rather well the SM expectations.

The final cut that has been made on the MHT trigger sample (Fig. 5.27) is to require two b-tags.

Table 5.4: Pretag cuts flow for MHT triggers.

Cut description	Data	signal(acceptance), M_{LQ3}=150 GeV
Trigger, $\not\!\!E_T$ >40 GeV, $\Delta\phi(\not\!\!E_T$,jet) >0.5	482635	310(62.9%)
$\not\!\!H_T > 40$ GeV	445280	306(62.0%)
1^{st} leading jet $E_T > 40$ GeV	419451	303(61.5%)
2^{nd} leading jet $E_T > 20$ GeV	167601	260(52.8%)
no bad jets $E_T > 15$ GeV	91568	251(50.9%)
the primary vertex $\|z\| < 60$ cm	87873	247(50.1%)
1^{st} leading jet $\|\eta_{det}\| < 1.5$	69892	236(48.0%)
jet track confirmation	49494	227(46.0%)
no isolated EM objects $p_T > 5$ GeV	46569	224(45.5%)
no isolated *medium* muons $p_T > 5$ GeV	44498	222(45.1%)
no isolated *loose* muons $p_T > 10$ GeV	44198	222(45.1%)
muon $p_T^{max} < 200$ GeV	44153	222(45.1%)
$\Delta\phi(\not\!\!E_T$,jet) > 0.7	25348	207(42.0%)
acoplanarity > 165 degrees	24661	202(41.0%)
"noQCD", $\not\!\!E_T$ >70 GeV	2804	167(33.9%)
pretag cuts:		
$\Delta\phi(\not\!\!E_T$, 1^{st} leading jet) < 3.0	2218	147(29.9%)
$H_T > 110$ GeV	1439	137(27.7%)
isolated track veto	1241	133(27.0%)

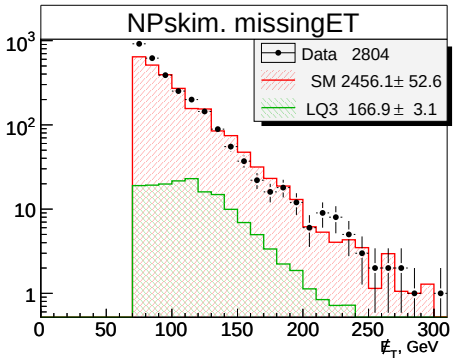

Figure 5.20: $\not\!\!E_T$.

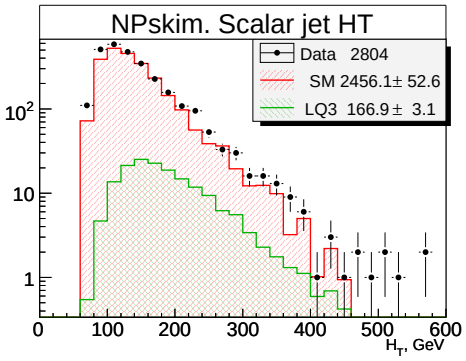

Figure 5.21: Scalar H_T.

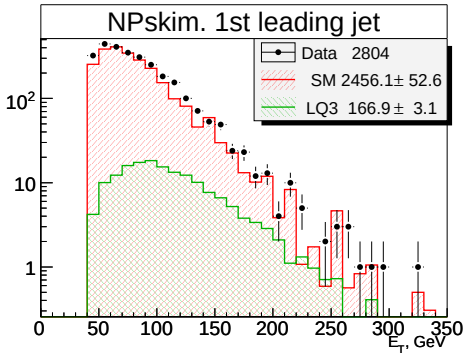

Figure 5.22: First leading jet E_T.

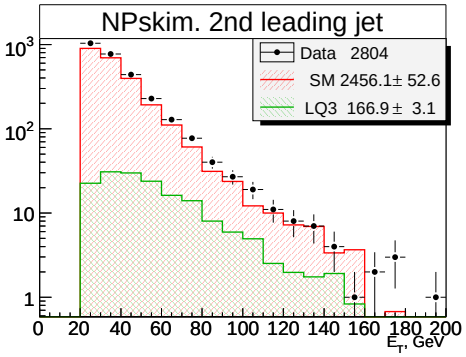

Figure 5.23: Second leading jet E_T

5.5.2 The JLIP tagger

The Jet Lifetime Probability b-tag algorithm (JLIP) [26] uses the fact that tracks originating from the secondary vertex have larger impact parameter than tracks from the primary vertex. Impact parameter is defined as the minimal distance from the primary vertex to a track in the plane transverse to the beam. It has the sign of the scalar product of the vector corresponding to it (starting from the primary

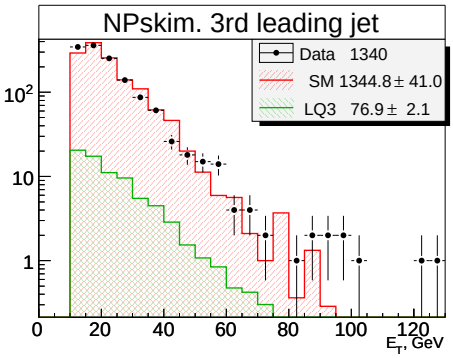

Figure 5.24: Third leading jet E_T.

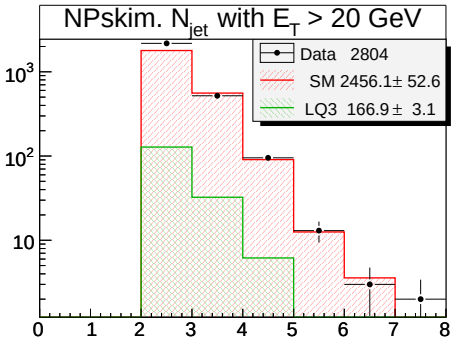

Figure 5.25: The number of jets $E_T >$ 20 GeV

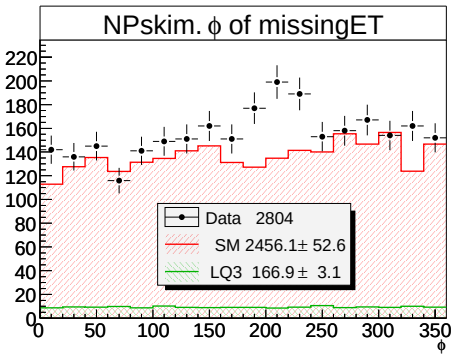

Figure 5.26: ϕ-distribution of $\not\!\!E_T$ at "noQCD" point.

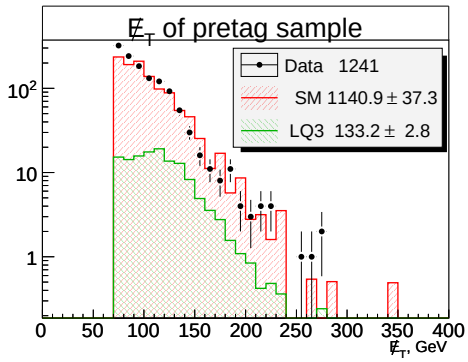

Figure 5.27: $\not\!\!E_T$ for the pretag sample.

vertex) with the track $\vec{p}_T$.

The impact parameter significance is defined as a ratio of the signed impact parameter to its error. The error depends on the track reconstruction quality and value of the multiple scattering of the charged particle in the volume of the tracker. The angle of the multiple scattering is proportional to the square root of path

length and inversely proportional to the particle momentum. In the plane transverse to the beam axis $p_T = p \cdot sin\theta$ and path $\sim sin\theta$. Thus, the effect of multiple scattering is incorporated in the variable $p_{scat} = p \cdot (sin\theta)^{3/2}$. The IP significance was parametrized in 16 p_{scat} intervals.

For every taggable jet[1] JLIP defines a probability $\mathcal{P}_{light}$ that all tracks in a jet originated from the primary vertex. For light quark jets this probability is uniformly distributed between 0 and 1, while for jets corresponding to heavy quark decay it peaks at very low values. A cut on the value $\mathcal{P}_{light}$ defines six working points of the JLIP algorithm:

- $ExtraLoose$: $\mathcal{P}_{light} < 0.04$
- $SuperLoose$: $\mathcal{P}_{light} < 0.02$
- $Loose$: $\mathcal{P}_{light} < 0.01$
- $Medium$: $\mathcal{P}_{light} < 0.005$
- $Tight$: $\mathcal{P}_{light} < 0.003$
- $UltraTight$: $\mathcal{P}_{light} < 0.001$

We performed direct tagging only on data. For Monte Carlo samples we obtained b-tag probabilities using the Tag Rate Function (TRF). The Tag Rate Function gives b-tag probabilities which depend on the E_T, η and jet flavor. The flavor of a MC jet can be found by matching the Monte Carlo hadrons with a jet cone. A MC jet is considered to be a b-jet if its cone contains at least one b-hadron.

[1] A jet is considered as taggable if it has at least two good quality tracks

If the jet cone does not match with a b-hadron, but matches with a c-hadron, the jet will be considered as a c-jet. If the jet cone does not match to a b or c hadron, it is considered as a light quark jet. Figures 5.28 and 5.29 qualitatively picture the $\mathcal{P}_{light}$ distribution and TFR for the data, signal and SM backgrounds.

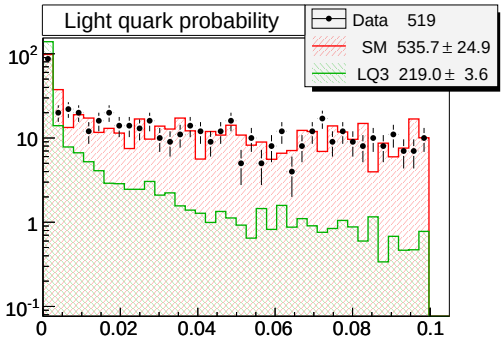

Figure 5.28: Distribution of $\mathcal{P}_{light}$.

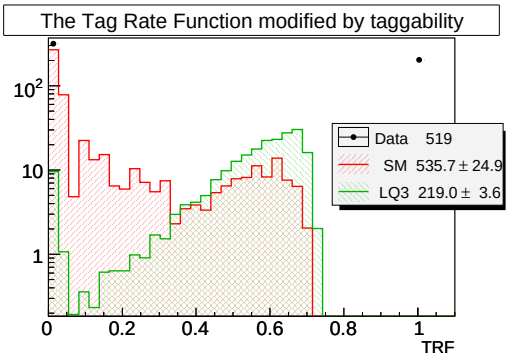

Figure 5.29: Tag Rate Function. (The data TRF is equal 0 or 1.)

The TRF should be multiplied by a factor called taggability. The taggability is defined as a probability of a jet to be taggable. It equals the ratio of the numbers of taggable jets to the total number of jets in given E_T and η bins. We also include in the determination of the taggability the z-position of the primary vertex for the event. Taggability is analysis-dependent and should be calculated for the data sample used for conditions which are close to that actually used for b-tagging. It is about 0.7 for the jets in this analysis. To parameterize the taggability we use jets with $E_T > 15$ GeV and $|\eta| < 2.5$ from events which passed the following cuts:

- $\Delta\phi(\not\!\!E_T, \text{jet } E_T > 15 \text{ GeV}) > 0.5$
- $\not\!\!E_T > 60$ GeV

- $\not\!\!E_T > 40$ GeV
- $E_{Tjet1} > 40$ GeV, $E_{Tjet2} > 20$ GeV,
- veto on events with isolated muons or EM objects.

Fig. 5.30 presents the E_T dependence of the jet taggability for this data sample. The solid line shows a fit to the data and the dashed lines show the error band after varying the fit error by $\pm 1\sigma$. Figures 5.31 and 5.32 show the corresponding dependence on η and z-position of the primary vertex. In Fig. 5.33 we compare the E_T distribution of taggable jets (points with error bars) with prediction based on the taggability fits for all three variables :

$$F(p_T, \eta, z_{PV}) = (\epsilon_{mean})^{-2} \times \epsilon(p_T) \times \epsilon(\eta) \times \epsilon(z_{PV})$$

Corresponding closure plots for the η of jets and for the z position of the primary vertex are presented in Figures 5.34 and 5.35. All closure plots show good agreement between real and predicted distributions. At the moment the JLIP package does not supply TRFs for the τ lepton which decay hadronically. We used the result of the sbottom analysis [28] where c-flavor TRFs were multiplied by a factor of 1.23 and the taggability multiplied by a factor of 0.55 to give the τ parameters.

Given the b-probability p_b = TRF(η, p_T,flavor) $\times$ taggability(η, p_T, z,flavor) for each taggable jet in the event, a probability for an event to have the required number of b-jets is calculated as usual. For example, the probability to have at least one b-jet in an event with n taggable jets is $w_1 = 1 - \sum_{i=1}^{n}(1 - p_{bi})$. This number should be used for the weighting of the event. To incorporate the cut $X_{jj} > 0.8$ (see Chapter 5.1.1) into b-tag result we compute X_{jj}^{perm} for each jets permutation

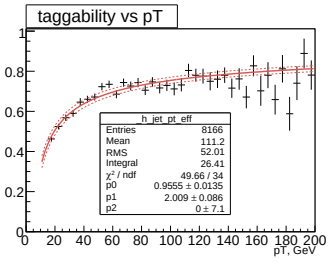

Figure 5.30: Taggability vs jet E_T

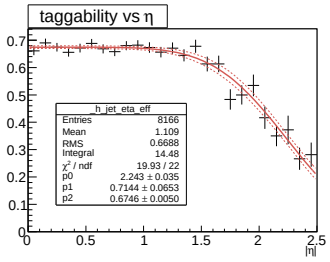

Figure 5.31: Taggability vs jet η

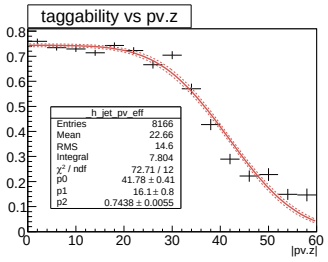

Figure 5.32: Taggability vs z of the primary vertex

.

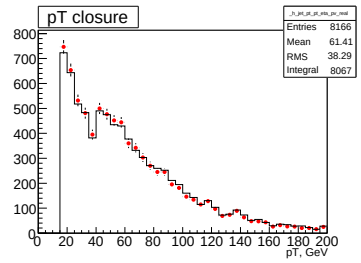

Figure 5.33: Closure plot, jet E_T

.

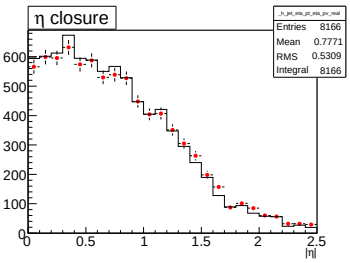

Figure 5.34: Closure plot, jet η

.

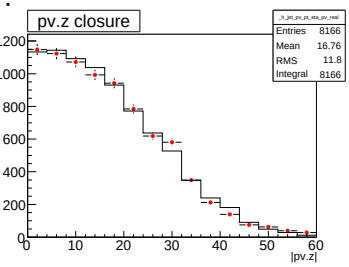

Figure 5.35: Closure plot, z of the primary vertex

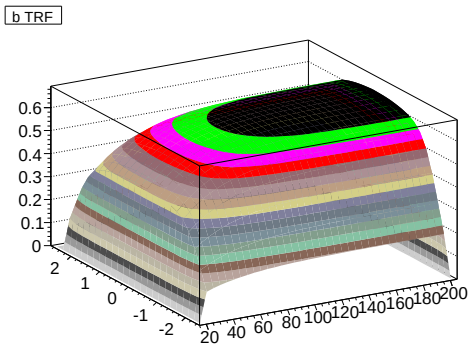

Figure 5.36: TRF for b flavor.

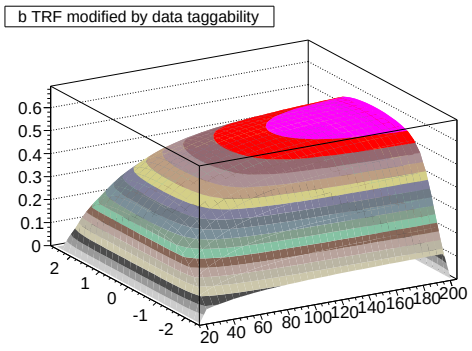

Figure 5.37: TRF for b flavor, modified by data taggability.

and use it to event weight the sum over permutations that have $X_{jj}^{perm} > 0.8$ only.

Following the signal signature, we required two b-jets in the event (double b-tag). Results for all the certified JLIP working points are listed in Table 5.5. The double *SuperLoose* b-tag appears to be the most favorable. Predicted contributions from Standard Model processes are listed in Table 5.6[1]. The largest contributions come from W and $Z + b\bar{b}$ production and top quark signal, as expected. The *SuperLoose* working point shows the best results in terms of the $S/\sqrt{B}$ ratio and the expected 95% CL cross-section limit. The 95% CL limits were obtained using the modified frequentalist approach [27] with correlations among systematic errors taken into account.

For LQ masses above 170 GeV cuts on $\not\!\!E_T$ and H_T were optimized by scanning the $\not\!\!E_T$-H_T space. The point that gave the best expected[2] cross-section limit was chosen. In the case of any ambiguity the point with the bigger signal acceptance was preferred. Table 5.7 show the scan result for $M_{LQ} = 220$ GeV. The cuts $\not\!\!E_T >$ 90 GeV and $H_T > 170$ GeV are optimal for both LQ masses 200 GeV and 220 GeV. The cross-section limits obtained using only the JLIP b-tag method are listed in Table 5.8.

[1]Sources of the systematic errors are discussed below in Section 5.8

[2]For the expected limit the number of data events is assumed equal to the number of events predicted by the Standard Model background.

Table 5.5: JLIP double tag for all working points, $M_{LQ3} = 150$ GeV

Tag	Data	SM±stat±sys	Signal±stat±sys	Accept., %	S/$\sqrt{B}$	σ_{exp}, pb
noQCD	1241	1141±37±282	133 ±2.8±15.6	27.0±2.7	3.9	2.24
ExtraLoose	8	6.90±0.32±1.90	37.62±0.96±7.62	7.6±1.5	14.3	0.40
SuperLoose	4	4.49±0.23±1.25	32.28±0.83±6.86	6.6±1.3	15.2	0.36
Loose	2	3.21±0.18±0.92	26.95±0.70±6.25	5.5±1.2	15.0	0.40
Medium	2	2.37±0.14±0.68	21.75±0.57±5.01	4.4±1.0	14.1	0.42
Tight	2	1.94±0.12±0.56	18.54±0.49±4.38	3.8±0.9	13.3	0.51
UltraTight	0	1.26±0.08±0.37	12.87±0.34±3.22	2.6±0.6	11.5	0.59

Table 5.6: JLIP *SuperLoose* double tag.

Process	Pretag	*SuperLoose* double tag
$W \to \mu\nu$+ jj	92.8 ± 5.2	0.16 ± 0.08
$W \to e\nu$+ jj	138 ± 12	0.06 ± 0.01
$W \to \tau\nu$+jj	342 ± 31	0.40 ± 0.06
$Z \to \nu\bar{\nu}$+ jj	519 ± 15	0.42 ± 0.16
top	36.4 ± 0.8	1.26 ± 0.07
$W/Z + b\bar{b}$	12.7 ± 0.6	1.90 ± 0.12
total MC	1141 ± 37	4.5 ± 0.2
data	1241	4
Signal (acceptance, %),		
$M_{LQ3} = 150$ GeV	133 ± 3 (27)	32.3 ± 0.8 (6.5)

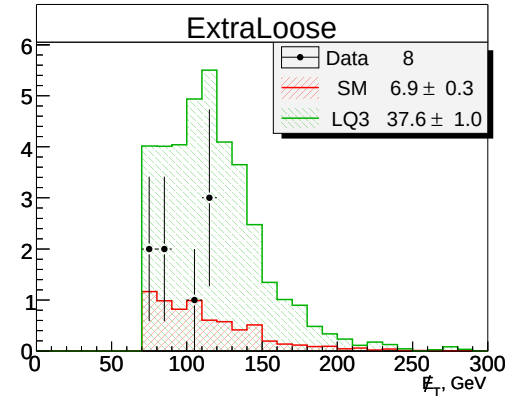

a) Double *ExtraLoose*

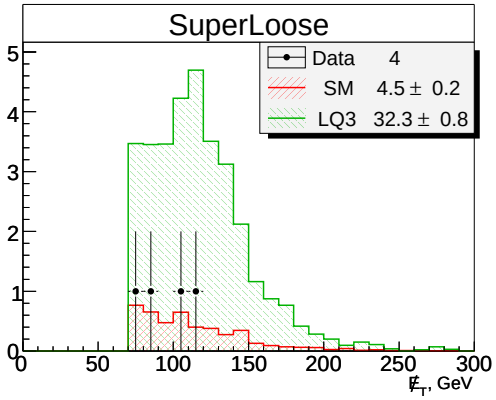

b) Double *SuperLoose*

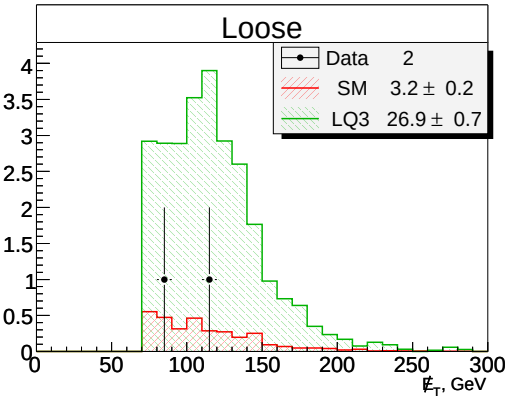

c) Double *Loose*

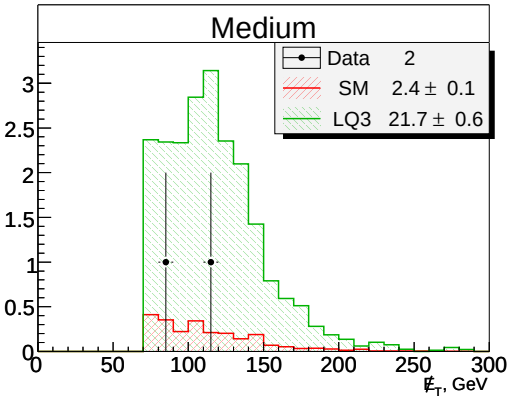

d) Double *Medium*

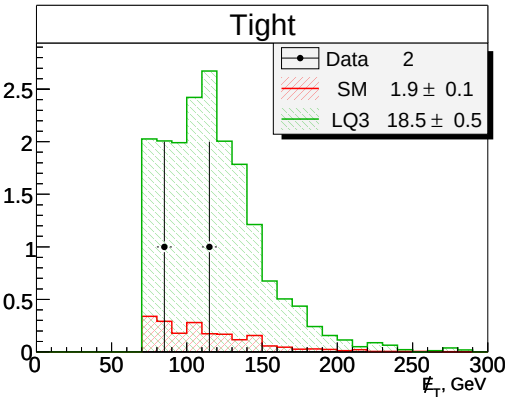

e) Double *Tight*

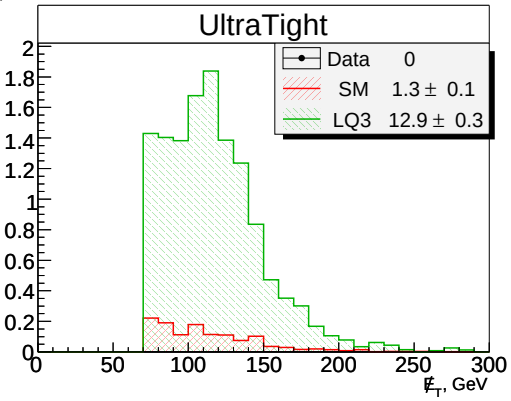

f) Double *UltraTight*

Figure 5.38: $\not\!\!E_T$ distributions with two b-tag for JLIP working points.

Table 5.7: Expected limits (pb) for $\not\!\!E_T - H_T$ scan for JLIP double b-tag, M_{LQ3}=220 GeV

H_T, GeV / $\not\!\!E_T$, GeV	110	120	130	140	150	160	**170**	180	190	200	210
80	0.23	0.20	0.21	0.22	0.18	0.20	0.21	0.18	0.19	0.20	0.22
90	0.21	0.22	0.18	0.19	0.20	0.21	**0.17**	0.19	0.20	0.22	0.24
100	0.20	0.20	0.20	0.21	0.22	0.18	0.19	0.20	0.22	0.24	0.26
110	0.22	0.22	0.23	0.18	0.19	0.20	0.21	0.22	0.24	0.26	0.20
120	0.20	0.20	0.20	0.20	0.20	0.21	0.23	0.24	0.26	0.20	0.21

Table 5.8: 95% CL cross-section limits for JLIP double b-tag

M(LQ3)	$\not\!\!E_T$,GeV	H_T,GeV	Data	SM$\pm$ stat $\pm$ sys	LQ3(acpt,%)	σ obs/exp, pb
150	70	110	4	4.49 $\pm$ 0.23 $\pm$ 1.25	6.55 $\pm$ 1.33	0.36 / 0.36
160	70	110	4	4.49 $\pm$ 0.23 $\pm$ 1.25	7.29 $\pm$ 1.45	0.32 / 0.32
170	70	110	4	4.49 $\pm$ 0.23 $\pm$ 1.25	8.26 $\pm$ 1.68	0.28 / 0.28
200	90	170	1	1.51 $\pm$ 0.10 $\pm$ 0.48	7.18 $\pm$ 1.65	0.21 / 0.21
220	90	170	1	1.51 $\pm$ 0.10 $\pm$ 0.48	8.52 $\pm$ 1.93	0.17 / 0.17

5.6 Muon Tagging Analysis

A muon emerging from the semileptonic decay of a heavy quark can be used for the selection of a b-jet. This section uses only muons to tag b-jets. We defined two different muon channels: single muon and dimuon. Events in the dimuon channel must contain at least two muons with B/C-layer segments and $p_T > 4$ GeV. We refer to the leading muon as the *primary*, and the next one as the *secondary*. If the event failed the dimuon criteria but it contains a muon with a B/C-layer segment and $p_T > 6$ GeV, it will be considered as a single muon channel event. These requirements are chosen to optimize a balance between the signal acceptance and the background rate. The application of a B/C-layer requirement for the *secondary* muon is intended to suppress the contribution of fake muons. In the dimuon channel we expect the background to be much smaller, which allows us to apply looser cuts. In the single muon channel we expect $W \rightarrow \mu\nu$ + jets to be the main background while in the dimuon channel top production dominates.

5.6.1 Single muon channel

We start the analysis of the single muon channel at the "noQCD" point (Table 5.4) and require the presence of a *primary* muon (not accompanied by a *secondary*). In addition, following our $W \rightarrow \mu\nu$ study, in order to guarantee the validity of the ALPGEN+PYTHIA MC samples used, we require that E_T of the second leading jet be > 25 GeV (see Fig. B.14).

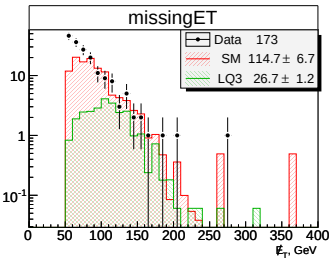

Figure 5.39: Marginal distribution of the $\not\!\!E_T$ for the "noQCD" sample for the single muon channel. $M_{LQ3} = 150$ GeV.

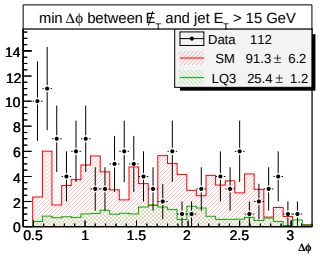

Figure 5.40: Marginal distribution of the $\Delta\phi$ between $\not\!\!E_T$ and nearest jet with $E_T > 15$ GeV in the "noQCD" sample for the single muon channel. $M_{LQ3} = 150$ GeV.

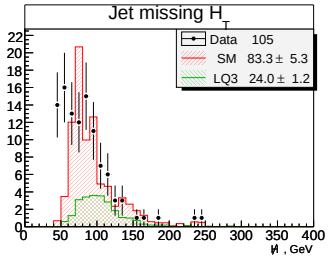

Figure 5.41: $\not\!\!H_T$ in the "noQCD" sample for the single muon channel. $M_{LQ3} = 150$ GeV.

Figures 5.39 and 5.40 show "marginal" distributions for $\not\!\!E_T$ and for $\Delta\phi$ between the $\not\!\!E_T$ direction and the nearest jet with $E_T > 15$ GeV. The marginal distribution are used to understand the variable as they have all the cuts applied except for the cut on the considered variable. The $\not\!\!E_T$ spectrum and jet multiplicity under these conditions are presented in Fig. 5.42 and Fig. 5.43. Results of the Xjj cut are presented in Fig. 5.44.

We applied an additional cleaning cut $\not\!\!H_T > 50$ GeV to remove the instrumental background contribution (Fig. 5.41). Because signal events tend to be more central, we required the second leading jet to have $|\eta_{det}| < 1.5$. This also forces it to be track confirmed. The distribution of $|\eta_{det}|$ of the second leading jet is presented in Fig. 5.45.

To suppress the contribution of muons from W decay which accidentally were associated with a jet, we used isolation cuts based on the tracking and calorimeter

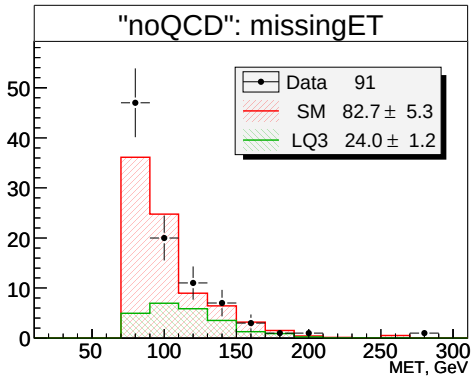

Figure 5.42: $\not\!\!E_T$ for the muon "noQCD" sample. $M_{LQ3} = 150$ GeV.

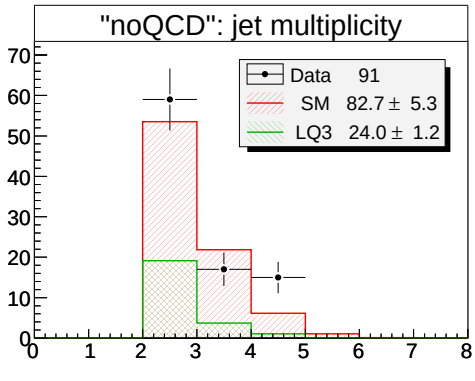

Figure 5.43: The number of jets with $E_T > 20$ GeV for the muon "noQCD" sample before the Xjj cut. $M_{LQ3} = 150$ GeV.

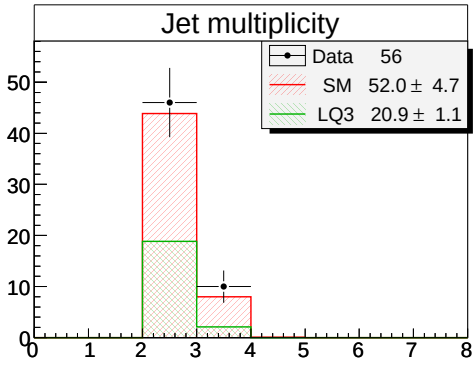

Figure 5.44: The number of jets with $E_T > 20$ GeV for the muon "noQCD" sample after the Xjj cut. $M_{LQ3} = 150$ GeV.

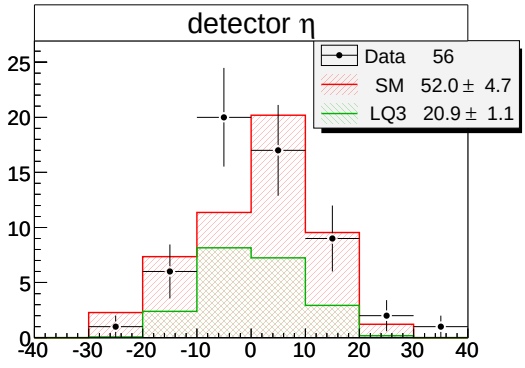

Figure 5.45: $|\eta_{det}|$ of the 2nd leading jet after the Xjj cut. $M_{LQ3} = 150$ GeV.

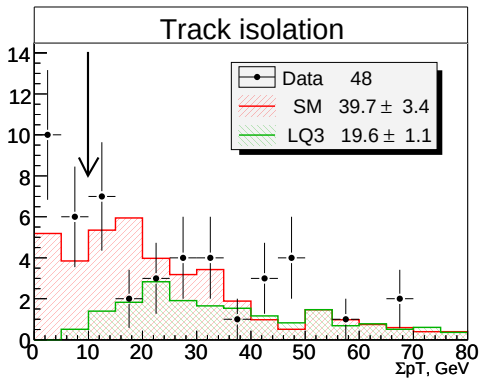

Figure 5.46: Sum of p_T of tracks in a cone of 0.5 around the muon after the cut on $|\eta_{det}|$ of the 2nd leading jet. $M_{LQ3} = 150$ GeV.

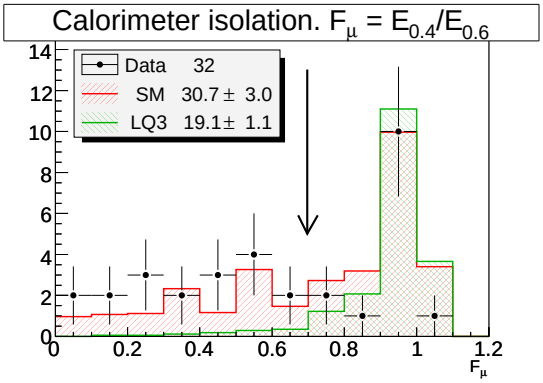

Figure 5.47: Calorimeter isolation. Ratio of the calorimeter energy in the cone of 0.4 to one in a cone of 0.6 around the muon. $M_{LQ3} = 150$ GeV.

information. Fig. 5.46 shows the distribution of the p_T sum of tracks in a cone of 0.5 around the muon. To calculate it we used tracks which satisfy the same criteria as tracks for jet track confirmation. We required $\Sigma_{tracks} p_T > 10$ GeV.

A muon from semileptonic decay points to a calorimeter region with a high energy deposition while a muon randomly associated with a jet does not have such a correlation. Correspondently, the ratio of the calorimeter energy in a cone of 0.4 to one in a cone of 0.6 around the muon coming from heavy quark decay should be close to 1. We denote this ratio as F_μ and require $F_\mu > 0.7$ (Fig.5.47).

As evident from the kinematics of semileptonic decay, more energetic leptons tend to be closer to the jet axis. We employ a simplified form of this and require $\Delta R \cdot p_T < 3.5$ GeV (Fig. 5.48).

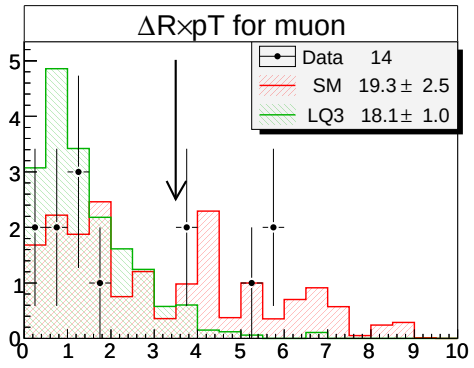

Figure 5.48: Product $\Delta R \cdot p_T$ for primary muon after the cut on track isolation. $M_{LQ3} = 150$ GeV.

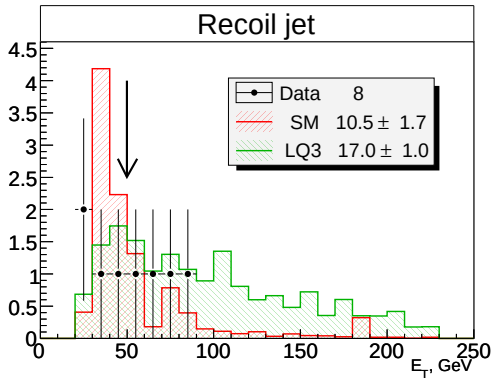

Figure 5.49: Recoil jet before cut. $M_{LQ3} = 150$ GeV.

Finally, we cut on the highest E_T jet in the event beside the muon jet ("recoil" jet) at 60 GeV. The distribution of the recoil jet before this cut is presented in Fig. 5.49.

After all cuts using only muon b-tags, we ended up with 4 events in data and 3.7 ± 0.9(stat) background events. The signal acceptance for the 13.1 ± 0.9(stat) signal events which survived the cuts is 0.027. Distributions of $\not\!\!E_T$ and jet multiplicity after all cuts are shown in Fig. 5.50 and Fig. 5.51. The cut flow for the single muon channel is summarized in Table. 5.9. $W \rightarrow \mu\nu + jets$ is still the main background: 1.7 events out of 3.7 total background. The remaining events of the background come from top or b-jets associated with W or Z production. Fig. 5.52 shows the parents of surviving muons for our MC samples.

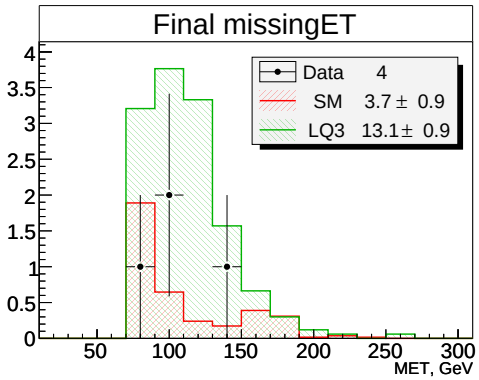

Figure 5.50: Single muon channel. $\not\!\!E_T$ after all cuts. $M_{LQ3} = 150$ GeV.

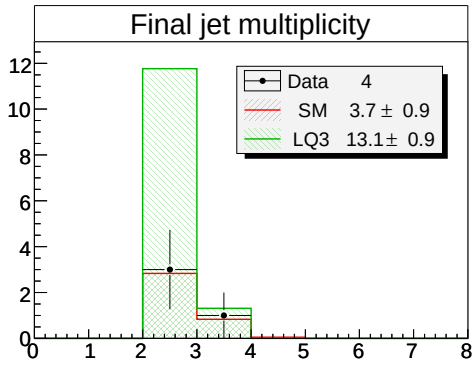

Figure 5.51: Single muon channel. The number of jets with $E_T > 20$ GeV after all cuts. $M_{LQ3} = 150$ GeV.

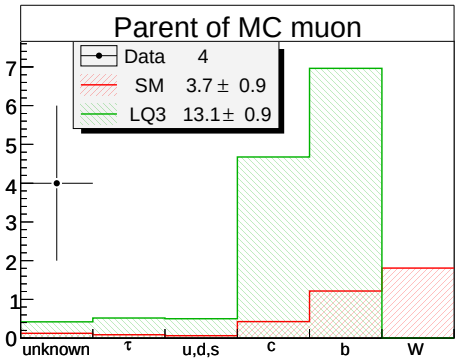

Figure 5.52: Single muon channel after all cuts. Parent of MC muon. $M_{LQ3} = 150$ GeV.

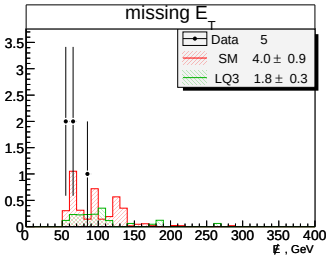

Figure 5.53: Marginal distribution of $\not\!\!E_T$ for the "noQCD" sample for the dimuon channel. $M_{LQ3} =$ 150 GeV.

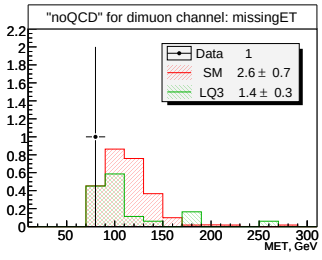

Figure 5.54: $\not\!\!E_T$ for the "noQCD" sample for the dimuon channel. $M_{LQ3} =$ 150 GeV.

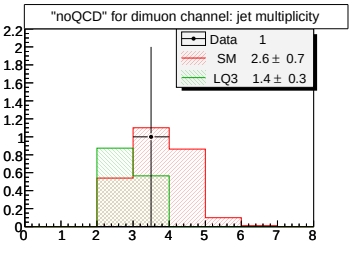

Figure 5.55: The number of jets with $E_T > 20$ GeV for the "noQCD" sample for the dimuon channel. $M_{LQ3} = 150$ GeV.

5.6.2 Dimuon channel

For the dimuon channel we required two muons, each with a B/C segment and with $p_T > 4$ GeV. In the dimuon channel we did not apply isolation requirements for the muons. We left the cut $\not\!\!E_T > 70$ GeV the same as in the single muon channel. Marginal distributions of $\not\!\!E_T$ in Fig. 5.53 explain our choice.

Only 1 data event satisfies the initial criteria for the dimuon channel. Figures 5.54 and 5.55 show $\not\!\!E_T$ and jet multiplicity distributions. After the Xjj cut no data events survived while the background was determined to be 0.6 events. Fig. 5.56 shows the resulting $\not\!\!E_T$ distribution. Table 5.10 gives the details for the samples used.

5.6.3 Combined result for muon tagging

Table 5.11 summarizes the results on both muon tagging channels for $M_{LQ} =$ 150 GeV. We obtained a combined limit on the sum of both muon channels for

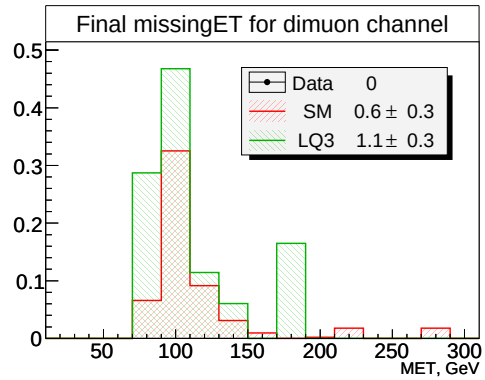

Figure 5.56: $\not\!\!E_T$ after the X_{jj} cut for the dimuon channel. $M_{LQ3} = 150$ GeV.

leptoquark with mass 150 GeV of $\sigma(LQLQ \to b\bar{b}\nu\bar{\nu}) < 0.75\ pb$ at 95% CL. Results for all signal samples are listed in Table 5.12.

Table 5.9: Cut flow for the single muon channel.

	noQCD	$p_{T\mu} > 6$	X_{jj}	$\lvert\eta_{det}\rvert$	Σp_T^{tr}	$F\mu$	$\Delta R \cdot p_T$	E_{Trjet}
data	109	91	56	48	32	14	8	4
LQ3, M=150	29.3	24.0	20.9	19.6	19.1	18.1	17.0	13.1
LQ3, M=200	7.21	5.75	4.96	4.78	4.56	4.37	3.95	3.39
LQ3, M=220	4.31	3.33	2.95	2.75	2.67	2.58	2.38	2.11
$W \to \mu\nu jj$	56.7	55.2	36.0	29.0	21.0	11.3	5.24	1.74
$W \to e\nu jj$	4.04	1.05	1.05	1.05	1.05	1.05	0	0
$W \to \tau\nu jj$	2.81	2.81	2.81	0	0	0	0	0
$Z \to \nu\nu jj$	14.4	8.94	7.26	5.35	4.86	4.12	3.23	0.456
$t\bar{t} \to l\nu jets$	11.6	9.19	1.58	1.51	1.35	1.04	0.616	0.563
$t\bar{t} \to l\nu l\nu$	2.00	1.55	0.585	0.564	0.484	0.277	0.176	0.151
$bt \to b\bar{b}\mu\nu$	0.525	0.422	0.267	0.242	0.210	0.167	0.122	0.099
$bt \to bq\bar{b}\mu\nu$	0.731	0.618	0.255	0.221	0.177	0.112	0.088	0.058
$bt \to bq\bar{b}e\nu$	0.166	0.125	0.059	0.052	0.049	0.039	0.039	0.032
$W \to \mu\nu b\bar{b}$	0.838	0.751	0.544	0.483	0.365	0.167	0.129	0.050
$W \to e\nu b\bar{b}$	0.404	0.360	0.264	0.246	0.219	0.218	0.194	0.122
$W \to \tau\nu b\bar{b}$	1.08	0.874	0.636	0.547	0.486	0.352	0.307	0.219
$Z/\gamma \to \nu\nu b\bar{b}$	1.18	0.751	0.602	0.515	0.485	0.438	0.404	0.232
total SM	96.5	82.7	52.0	39.7	30.7	19.3	10.5	3.72
error $\pm$	5.81	5.32	4.71	3.37	3.01	2.47	1.71	0.863
ϵ_{LQ}, % M=150	5.94	4.87	4.25	3.99	3.88	3.66	3.44	2.65
ϵ_{LQ}, % M=200	8.68	6.92	5.97	5.76	5.49	5.26	4.75	4.08
ϵ_{LQ}, % M=220	9.87	7.62	6.75	6.30	6.11	5.89	5.44	4.82

Table 5.10: Cut flow for the dimuon channel.

	noQCD	dimuon channel	$p_{T1,2} > 4$ GeV, B/C segment	$X_{jj} > 0.8$
data	109	8.00	1.00	0
LQ3, M=150 GeV	29.3	5.85	1.44	1.09
LQ3, M=200 GeV	7.21	1.32	0.455	0.371
LQ3, M=220 GeV	4.31	0.912	0.261	0.205
$W \rightarrow \mu\nu jj$	56.7	6.02	0.904	0.302
$W \rightarrow e\nu jj$	4.04	0	0	0
$W \rightarrow \tau\nu jj$	2.81	0	0	0
$Z \rightarrow \nu\nu jj$	14.4	0.961	0.490	0
$t\bar{t} \rightarrow l\nu jets$	11.6	2.92	0.787	0.099
$t\bar{t} \rightarrow l\nu l\nu$	2.00	0.498	0.189	0.041
$bt \rightarrow b\bar{b}\mu\nu$	0.525	0.117	0.053	0.026
$bt \rightarrow bq\bar{b}\mu\nu$	0.731	0.157	0.057	0.015
$bt \rightarrow bq\bar{b}e\nu$	0.166	0.014	0.003	0.003
$W \rightarrow \mu\nu b\bar{b}$	0.838	0.057	0.022	0
$W \rightarrow e\nu b\bar{b}$	0.404	0.100	0	0
$W \rightarrow \tau\nu b\bar{b}$	1.08	0.089	0.045	0.045
$Z/\gamma \rightarrow \nu\nu b\bar{b}$	1.18	0.228	0.064	0.030
total SM	96.5	11.2	2.61	0.561
error $\pm$	5.81	1.47	0.729	0.310
ϵ_{LQ}, M=150 GeV %	5.94	1.19	0.292	0.222
ϵ_{LQ}, M=200 GeV %	8.68	1.59	0.547	0.447
ϵ_{LQ}, M=220 GeV %	9.87	2.09	0.597	0.469

Table 5.11: Summary for both muon channels. $M_{LQ3} = 150$ GeV

	single	dimuon	total
Data	4	0	4
SM	3.72	0.56	4.3
SM stat err	0.86	0.31	0.9
SM sys err	0.92	0.11	1.0
Signal	13.1	1.09	14.2
Signal stat err	0.88	0.25	0.9
Signal sys err	1.30	0.11	1.4
Signal acceptance	0.0265	0.0022	0.0288
Signal acceptance err	0.0027	0.0005	0.0028

Table 5.12: Summary for all signal samples for the muon tagging.

M_{LQ3}, GeV	Data	SM ± stat ± sys	Signal ± stat ± sys	Acceptance, %	σ, pb
150	4	4.28 ± 0.92 ± 1.01	14.17 ± 0.91 ± 1.05	2.88 ± 0.28	0.75
160	4	4.28 ± 0.92 ± 1.01	11.28 ± 0.57 ± 1.00	3.37 ± 0.34	0.64
170	4	4.28 ± 0.92 ± 1.01	8.28 ± 0.41 ± 0.65	3.57 ± 0.33	0.60
200	4	4.28 ± 0.92 ± 1.01	3.76 ± 0.20 ± 0.25	4.53 ± 0.39	0.47
220	4	4.28 ± 0.92 ± 1.01	2.31 ± 0.12 ± 0.15	5.29 ± 0.44	0.40

5.7 Combining the Muon and JLIP Taggers

We have combined the results of the muon and JLIP tagging analysis for MHT triggered events. The *SuperLoose* JLIP criteria was used for the combination. We prepared for JLIP b-tagging subsamples of the data, signal and SM, which do not contain events which passed the selection criteria for either of the muon channels. Thus, each event was processed by the JLIP analysis or in one of the muon channels only. The results of the double JLIP b-tag of non-muon events are listed in Table 5.13.

A single JLIP b-tag was applied to all muon tagged events (JLIP b-tag was required also for dimuon events to reduce the contribution of events with muons from K/π decays). An application of a JLIP b-tag allowed us to decrease the irreducible muon tagging background $W \to \mu\nu$ from 2.04 to 0.15 events. The total expected contribution of Standard Model processes was decreased by 65% while the lost of signal ($M_{LQ} = 200$ GeV) was 20%. No data events survived the combination of muon and JLIP b-tag. Table 5.14 lists results for muon tagging plus single JLIP b-tag for all signal samples. The efficiency of muon tagging plus single JLIP tag for signal ($M_{LQ} = 200$ GeV) was 49.1%, while application of the same event selection which was used for the non-muon sample would result in an efficiency of only 26.6%. The application for muon events of muon tagging plus single JLIP tag instead of double b-tag selection results in an additional 1.9 signal events or 2.3% in additional acceptance. The contribution of the expected SM also increase (from

0.3 to 1.5 events), but the $S/\sqrt{B}$ ratio was improved from 2.0 to 2.5.

Table 5.15 presents the final results. The choice of cuts on $\not\!\!E_T$ and H_T is illustrated in Table 5.16. Comparing this to the results of applying just the JLIP double b-tag to the MHT sample (Table 5.8, M_{LQ} =220 GeV), we increased the signal acceptance by 46%. It gave a corresponding improvement of 12% in the 95% CL cross-section limit for this LQ3 mass point.

Table 5.13: Summary for JLIP subsamples without muon events

M_{LQ3} GeV	$\not\!\!E_T$ GeV	H_T GeV	Data	SM ± stat ± sys	Signal ± stat ± sys	Acceptance, %
150	70	110	4	4.24 ± 0.23 ± 1.19	32.28 ± 0.83 ± 6.86	6.55 ± 1.34
160	70	110	4	4.24 ± 0.23 ± 1.19	24.40 ± 0.51 ± 5.09	7.29 ± 1.45
170	70	110	4	4.24 ± 0.23 ± 1.19	19.15 ± 0.38 ± 4.07	8.26 ± 1.68
200	90	150	1	1.94 ± 0.17 ± 0.60	5.64 ± 0.15 ± 1.33	6.79 ± 1.54
220	90	190	1	1.04 ± 0.08 ± 0.37	3.53 ± 0.09 ± 0.80	8.07 ± 1.78

Table 5.14: Muon + single JLIP b-tag. $\not\!\!E_T$ >70 GeV, no cut on H_T.

M_{LQ3}(GeV)	Data	SM ± stat ± sys	Signal ± stat ± sys	Accept., %	σ, pb obs/exp
150	0	1.52 ± 0.16 ± 0.34	11.28 ± 0.74 ± 1.24	2.29 ± 0.25	0.44 / 0.59
160	0	1.52 ± 0.16 ± 0.34	8.99 ± 0.46 ± 1.10	2.69 ± 0.31	0.38 / 0.51
170	0	1.52 ± 0.16 ± 0.34	6.66 ± 0.34 ± 0.75	2.87 ± 0.30	0.35 / 0.47
200	0	1.52 ± 0.16 ± 0.34	3.04 ± 0.16 ± 0.32	3.66 ± 0.36	0.27 / 0.37
220	0	1.52 ± 0.16 ± 0.34	1.86 ± 0.10 ± 0.19	4.27 ± 0.41	0.24 / 0.32

Table 5.15: 95% CL limits ($310 pb^{-1}$) for MUON + JLIP tagging analysis.

M_{LQ3} GeV	($\not\!\!E_T$ H_T)[a] GeV	Data	SM±stat±sys	LQ3±stat±sys	Accept. %	σ, pb obs/exp
150	(70, 110)	4	5.8 ± 0.3 ± 1.4	39.5±1.1±6.4	8.0±1.2	0.26 / 0.33
160	(70, 110)	4	5.8 ± 0.3 ± 1.4	30.1±0.7±4.8	9.0±1.3	0.23 / 0.29
170	(70, 110)	4	5.8 ± 0.3 ± 1.4	23.3±0.5±3.8	10.0±1.5	0.20 / 0.26
200	(90, 150)	1	3.5 ± 0.2 ± 0.8	8.7±0.2±1.4	10.5±1.6	0.12 / 0.18
220	(90, 190)	1	2.6 ± 0.2 ± 0.6	4.7±0.1±0.8	10.8±1.6	0.12 / 0.15

[a]applied to non-muon subsample only

Table 5.16: MUON + JLIP. Expected limit vs cuts on $\not\!\!E_T$ and H_T applied to non-muon subsample only. $M_{LQ} = 220$ GeV.

H_T / $\not\!\!E_T$	110	120	130	140	150	160	170	180	**190**	200	210
80	0.179	0.160	0.164	0.168	0.175	0.153	0.162	0.168	0.177	0.154	0.162
90	0.166	0.168	0.173	0.177	0.155	0.162	0.168	0.175	**0.152**	0.160	0.168
100	0.181	0.182	0.157	0.160	0.164	0.168	0.177	0.153	0.160	0.166	0.175
110	0.166	0.166	0.168	0.171	0.175	0.179	0.154	0.160	0.166	0.175	0.184
120	0.179	0.179	0.182	0.182	0.185	0.157	0.162	0.168	0.175	0.184	0.193

5.8 Systematic Errors

The error on integrated luminosity is taken from [29]. A 15% uncertainty was set on the cross-sections of the Standard Model samples. The systematics associated with the Jet Energy Scale corrections was estimated by varying the JES correction factor for each MC jet by

$$\sqrt{\sigma_{MC}^2 + \sigma_{DATA}^2},$$

where

$$\sigma_{MC} = \sqrt{(\sigma_{MC}^{sys})^2 + (\sigma_{MC}^{stat})^2},$$
$$\sigma_{DATA} = \sqrt{(\sigma_{DATA}^{sys})^2 + (\sigma_{DATA}^{stat})^2}$$

Changes in jet E_T due to the variation of the JES correction factor were propagated to all dependent variables like $\not\!\!E_T$, H_T, etc. The b-tag uncertainty was estimated by varying the b-tagging efficiency by $\pm 1\sigma_{btag}$, where σ_{btag} is uncertainty of the tag rate function. To obtain uncertainty on taggability we varied the fit error by $\pm 1\sigma_{tagg}$. For σ_{tagg} we took the errors on E_T-, η-, and z-dependencies added in quadrature. Sources of the uncertainties which were taken into account are summarized in Table 5.17. The numerical values of uncertainties correspond to the double JLIP b-tag analysis. To obtain the systematic uncertainties of the final result (Tab. 5.15) the uncertainties for muon and non-muon results were added in quadratures.

Table 5.17: Systematic uncertainties

Error source	%
Integrated luminosity	6.5
SM cross-section	15
Trigger efficiency	5
Track confirmation	1
JES systematic	
signal $M_{LQ} = 200$ GeV	+6.1, -8.7
SM background	+10.6, -14.3
Taggability	
signal $M_{LQ} = 200$ GeV	+4.5, -4.4
SM background	+5.0, -4.9
b-tagging	
signal $M_{LQ} = 200$ GeV	+19.7 , -16.6
SM background	+17.3 , -15.2

5.9 Mass Limits

Since we do not observe an excess in data over the expectations from the Standard Model, we have set upper limits on the cross-section for the pair production of scalar third generation leptoquarks. To establish lower limits on the leptoquark mass we found an intersection of the theory cross-section with the 95% CL experimental cross-section limits. We use the lower band of the theory production cross-section [8] corresponding to the renormalization scale $\mu = +2M_{LQ}$. The theory cross-section error band also includes PDF errors.

For $M_{LQ} > m_t + m_\tau$ the decay $LQ \to t\tau$ is also possible (m_t and m_τ are the masses of the *top*-quark and the τ-lepton, respectively). For $M_{LQ} \gg m_{top}$ we assume $B(LQ \to \nu b) = B(LQ \to t\tau) = 0.5$. For masses just above the threshold the $t\tau$ decay channel is suppressed by the phase space factor [16]

$$F_{sp} = \sqrt{((1 + d_1 - d_2)^2 - 4d_1)}[1 - (d_1 + d_2)/2 - (d_1 - d_2)^2/2],$$

where $d_1 = (m_t/M_{LQ})^2$ and $d_2 = (m_\tau/M_{LQ})^2$.

Thus, $B(LQ \to \nu b) = 1 - 0.5F_{sp}$.

The preliminary limits on leptoquark mass achieved in this analysis with the $B(LQ \to \nu b) = f(F_{sp})$ and with $B(LQ \to \nu b) = 1$ in parenthesis are:

- muon analysis alone - 170 (170) GeV
- muon plus the single *SuperLoose* *b*-tag - 190 (191) GeV
- double JLIP *b*-tag applied to the whole MHT dataset - 199 (202) GeV
- combination of muon and non-muon *b*-tagging - 213 (219) GeV

These results are in agreement with the scalar bottom quark search [28] (which have

a similar signal for the neutralino mass equal zero).

5.10 Summary

We have obtained limits at the 95% CL for the pair production cross-section of charge 1/3 third generation scalar leptoquarks for the decay mode $LQ\overline{LQ} \rightarrow \nu\bar{\nu}b\bar{b}$. Data collected with MHT triggers ($L_{eff} = 310\ pb^{-1}$) were analyzed separately using both muon and JLIP b-tagging. The number of events which passed our selection cuts agrees with the Standard Model expectations for both analyses. Double JLIP b-tag applied to the MHT-triggered sample established a 199 GeV limit on leptoquark mass. To improve it the muon tagged events were extracted from the dataset and were additionally required to have a single JLIP b-tag. The rest of the events required two JLIP b-tags. A combination of the results set a limit on the leptoquark mass of 213 GeV. A mass limit under the assumption of $B(LQ \rightarrow \nu b) = 1$ is equal to 219 GeV. The exclusion plot is shown in Fig. 5.57. The blue solid line with data dots shows the observed cross-section obtained using the actual number of events in data and the expected contribution of Standard Model processes. For comparison the blue dashed line shows the cross-section under the assumption that the number of events in data is equal to the expected number of events from SM Monte Carlo.

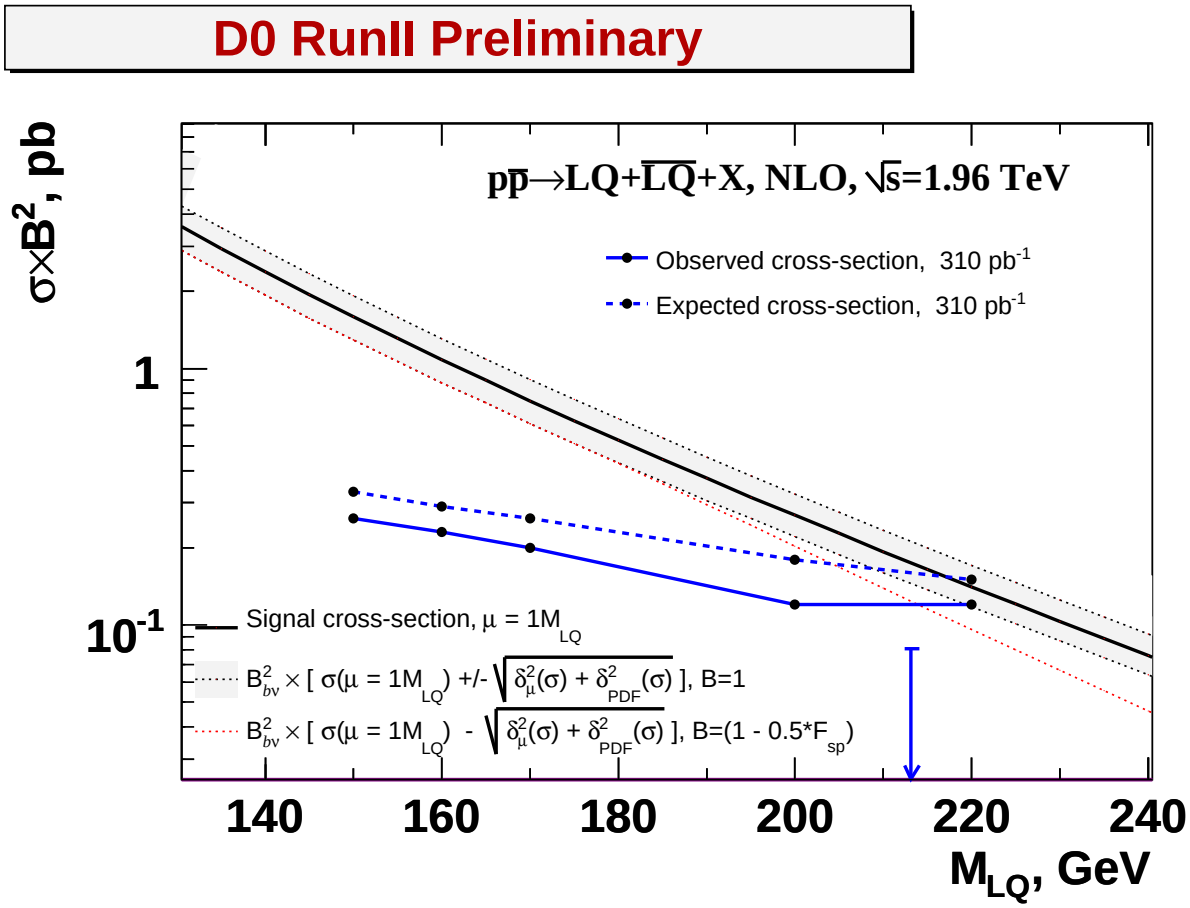

Figure 5.57: Exclusion plot. Cross section × (branching fraction (B))^2. The blue solid line with data dots is the observed cross-section. The blue dashed line is the expected cross-section (N_{data} is assumed equal to N_{SM}). The black solid line is theoretical cross-section with error band which includes variations of the renormalization scale and PDF uncertainties. The red dotted line shows the effect of the $LQ \to t\tau$ decay on the lower bound of the theory.

CHAPTER 6
CONCLUSION

A search for the pair production of scalar leptoquarks of the third generation was performed using 310 pb^{-1} of data collected by the DØ detector at the Tevatron $p\bar{p}$ collider. The explored topology 2 b-jets plus missing energy corresponds to the leptoquark decay channel $LQ \rightarrow b\nu$. Since no excess of data events over the Standard Model expectation was observed, a 95% confidence level upper limit on the leptoquark pair production cross-section was set to 0.12 pb (observed). To obtain a lower limit on the leptoquark mass, the suppression factor for the branching ratio of the concurrent decay channel $LQ \rightarrow t\tau$ was taken into account. The lower mass limit of 213 GeV corresponds to the excluded cross-section assuming the presence of both decay channels, while the mass limit of 219 GeV corresponds to the case that the branching fraction for $LQ \rightarrow b\nu$ is 100%.

The result was obtained by combining muon tagging with b-tagging based on the jet's impact parameter. Possible improvements that can be considered include

- application of identification of hadronic τ decays
- using b-tagging based on reconstruction of the secondary vertex
- lowering the muon momentum threshold in the single muon channel

- application of advanced analysis technique based on, for example, neural networks.

APPENDIX A
TRIGGER AND SKIM DEFINITIONS

A.1 $\not{H}_T$-based triggers used for the analysis

- **MHT30_3CJT5 trigger**

  L1: at least 3 calorimeter trigger towers with $E_T > 5$ GeV

  L2: Require $\not{H}_T \equiv \sum_{jets} |\vec{p_t}| > 20$ GeV

  L3: Vector $|\sum_{jets} \vec{p_t}| > 30$ GeV

- **JT1_ACO_MHT_HT trigger**

  L1: at least 3 calorimeter trigger towers with $E_T > 5$ GeV

L2: Require $\not\!\!H_T \equiv \sum_{jets} |\vec{p_t}| > 20$ GeV, acoplanarity[1] < 168.75 degrees

L3: Vector $|\sum_{jets} \vec{p_t}| > 30$ GeV, acoplanarity < 170.0 degrees, $H_T > 50$ GeV

A.2 SKIM Definition

An initial data sample ("skim") consists of events which satisfy one of the $\not\!\!H_T$-based trigger (MHT30_3CJT5, JT1_ACO_MHT_HT, JT2_MHT25_HT, MHT20_L2L0_PVZ). It also contains events that satisfied the prescaled trigger 3CJT5, which are added for monitoring purposes. The total number of events in the skim is 37648171.

For the present analysis we used only events which passed the criteria below

- good runs for muon, calorimeter, CFT, and SMT subsystem
- Luminosity blocks: satisfied to the requirements of the calorimeter and $\not\!\!E_T$ working groups

Data correspond to an effective luminosity of 310 pb^{-1}. The contributions of the particular triggers are shown in Table A.1.

Table A.1: Effective luminosities associated with different triggers (used for normalization of the SM MC samples)

Trigger	MHT30_3CJT5	JT1_ACO_MHT_HT
Luminosity	261 pb^{-1}	49 pb^{-1}

[1] the azimuthal angle between the two leading jets

APPENDIX B
ALPGEN MONTE-CARLO SAMPLES

We checked the validity of 2-jet MC samples using data events corresponding to $W \rightarrow \mu\nu + jets$. We did that in three steps:

• checked description of $W \rightarrow \mu\nu + jets$ events collected by the single muon trigger (to avoid possible ambiguity in parametrization of the MHT triggers)

• checked transition to the $\not\!\!H_T$ trigger on a subsample of muon data

• finally, checked description of total sample, which involves many Standard Model processes.

Selected $W \rightarrow \mu\nu + jets$ events correspond to 282.8 pb^{-1}. We selected W event candidates that passed the single muon trigger following the criteria described in section 5.4.4. To account for data - Monte Carlo differences in track-matching and isolation we applied to Monte Carlo a coefficient $0.936 \cdot 0.978 = 0.915$.

We obtained the muon trigger efficiency using data collected by $\not\!\!H_T$-based triggers. As expected, it is nearly constant for high p_T muons (Fig. B.1). Combining the value of the muon trigger efficiency 0.677 with the data-MC correction we got a total normalization factor of 0.62 for Monte Carlo.

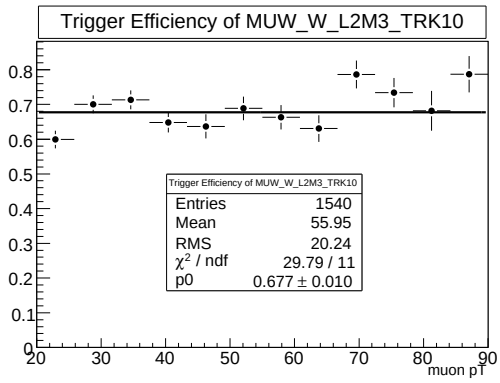

Figure B.1: Trigger efficiency of the single muon trigger.

Figures B.2 and B.3 show the transverse mass and muon p_T while Figures B.4 - B.7 present jet distributions. Vector $\not\!\!H_T$ and scalar H_T built out of jets are presented in figures B.8-B.9 while $\not\!\!E_T$ is shown in Fig. B.10. In general, we can conclude that 2-jet samples describe well clean data samples of $W \rightarrow \mu\nu + jets$ after cuts of 40 GeV on the leading jet and of 20 - 25 GeV on subleading jets.

Figures B.11-B.16 show a subsample of events in which the $\not\!\!H_T$-based trigger fired along with the single muon trigger. They show a smooth transition to $\not\!\!H_T$-based trigger without any additional normalization. We assume that the good description of clean signal $W \rightarrow \mu\nu + jets$ implies that similar Monte Carlo samples for other

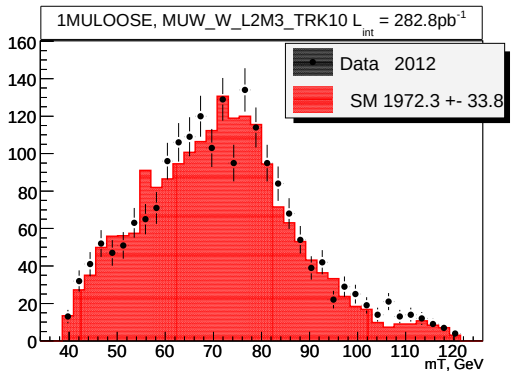

Figure B.2: Single muon trigger. Transverse mass.

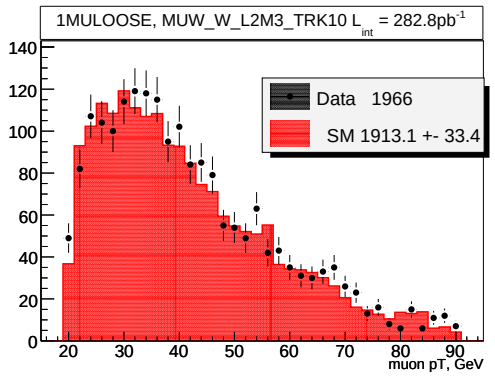

Figure B.3: Single muon trigger. Muon p_T.

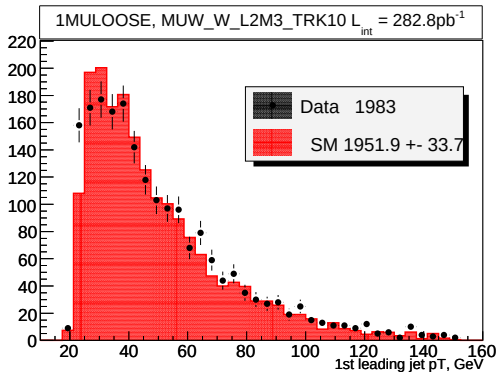

Figure B.4: Single muon trigger. 1st leading jet E_T.

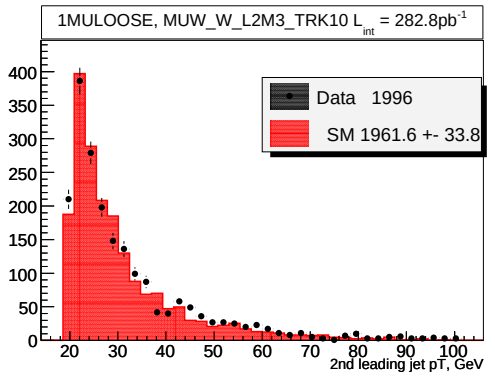

Figure B.5: Single muon trigger. 2nd leading jet E_T.

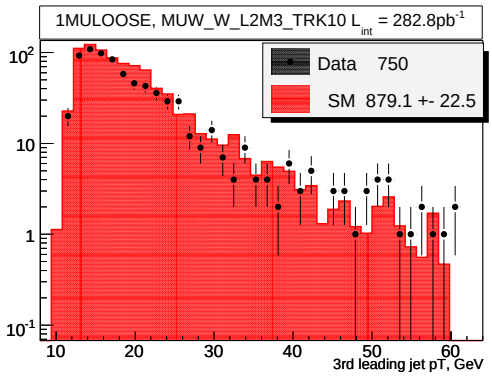

Figure B.6: Single muon trigger. 3rd leading jet E_T.

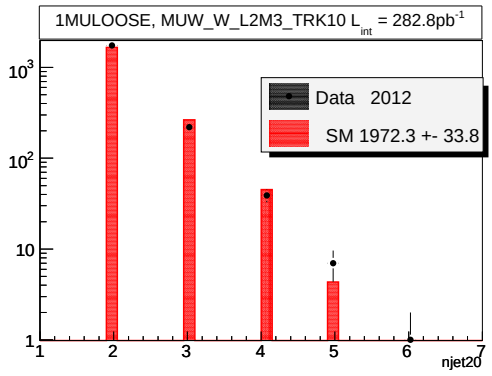

Figure B.7: Single muon trigger. The number of jets $E_T > 20$ GeV.

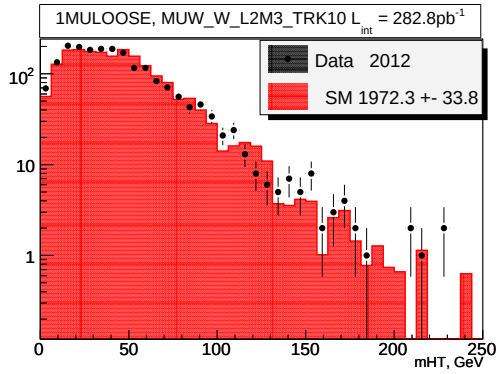

Figure B.8: Single muon trigger. Vector $\not{H}_T$.

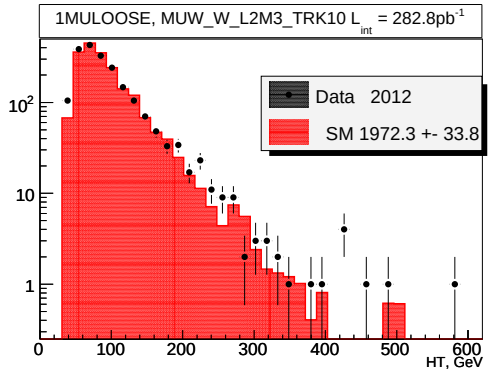

Figure B.9: Single muon trigger. Scalar H_T.

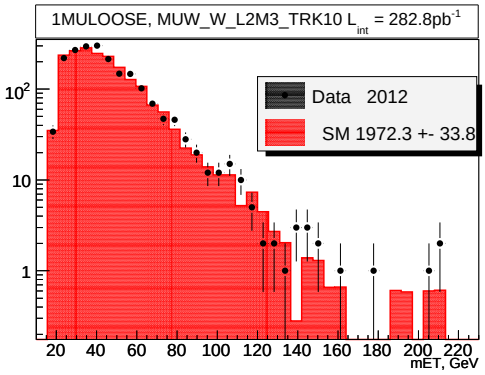

Figure B.10: Single muon trigger. $\not\!\!E_T$.

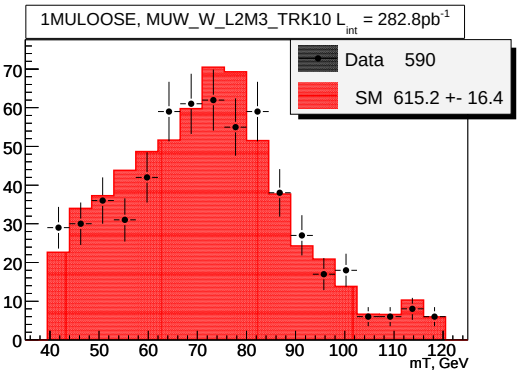

Figure B.11: Single muon trigger with $\not\!\!H_T$-based trigger. Transverse mass.

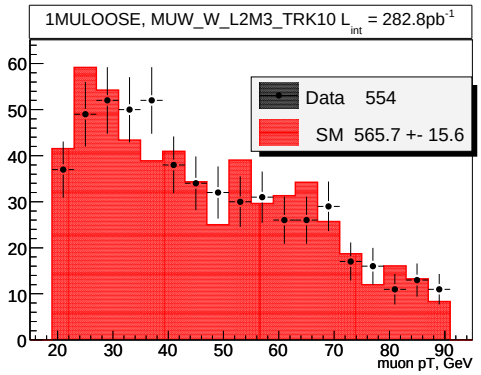

Figure B.12: Single muon trigger with $\not\!\!H_T$-based trigger. Muon p_T.

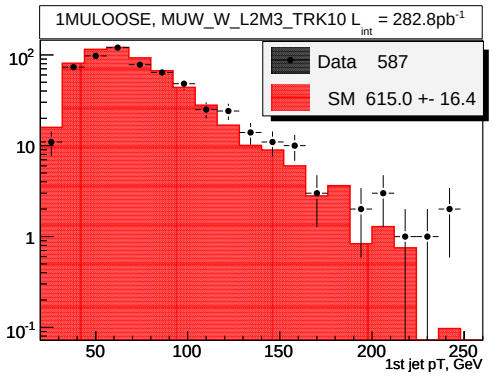

Figure B.13: Single muon trigger with $\not\!\!H_T$-based trigger. 1st leading jet E_T.

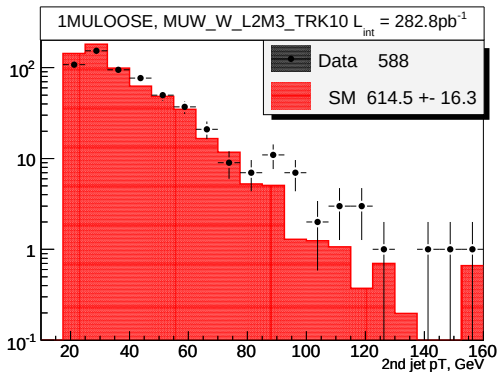

Figure B.14: Single muon trigger with $\not\!\!H_T$-based trigger. 2nd leading jet E_T.

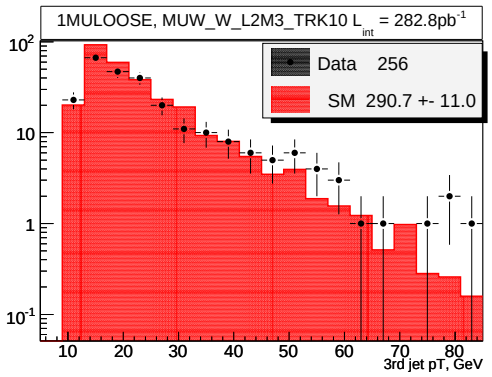

Figure B.15: Single muon trigger with $\not\!\!H_T$-based trigger. 3rd leading jet E_T.

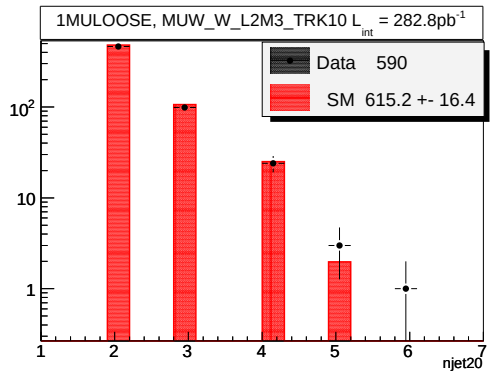

Figure B.16: Single muon trigger with $\not\!\!H_T$-based trigger. The number of jets $E_T > 20$ GeV.

leptons and Z boson can also be considered valid.

REFERENCES

[1] JoAnne L. Hewett and Thomas G. Rizzo, Much Ado About Leptoquarks: A Comprehensive Analysis, SLAC-PUB-7430, March 1997.

[2] S. Martin, A Supersymmetry Primer, hep-ph/9709356.

[3] J.C. Pati and A. Salam, Phys. Rev. D10, 275 (1974).

[4] J. Blumlein, E. Boos, A. Kryukov, "Leptoquark pair production in hadronic interactions," Z. Phys. C 76, 137-153 (1997).

[5] W. Buchmüller, R. Rückl, and D. Wyler, Phys. Lett. B191, 442 (1987).

[6] A. F. Zarnecki, "Leptoquark signal from global analysis," The European Physical Journal C **17**, 695-706 (2000).

[7] D. Acosta and S. Blessing, "Leptoquark Searches at Hera and the Tevatron," Annu. Rev. Nucl. Part. Sci. **49**, 389 (1999).

[8] M. Kramer, T. Plehn, M. Spira and P. M. Zerwas,"Pair production of scalar leptoquarks at the Tevatron," Phys. Rev. Lett. **79**, 341 (1997) [arXiv:http://arxiv.org/abs/hep-ph/9704322].

[9] M. Kuze and Y. Sirois, Search for Particles and Forces Beyond the Standard Model at HERA ep and TeVatron $p\bar{p}$ Colliders, DESY-02-165, arXiv:hep-ex/0211048 (2002).

[10] P. B. Straub, Minireview of Leptoquark Searches, to appear in the proceedings of 31st International Conference on High Energy Physics (ICHEP 2002), Amsterdam, The Netherlands, 24-31 Jul 2002, arXiv:hep-ex/0212023 (2002).

[11] V. M. Abazov *et.el.* [D0 Collaboration], Nucl. Instrum. Methods (to be published), arXiv:physics/0507191.

[12] Tim Christiansen, Ph.D Thesis, Ludwig-Maximilians-Universität Mïchenn, Germany (2002) (Unpublished).

[13] A. Zabi, L. Duflot, J.-F. Grivaz, P. Verdier, A. Duperrin, "A trigger for Jets and Missing E_T," D0 Note **4315** (2004).

[14] Adams D., "Finding Tracks," D0 Note **2958** (1996) (Unpublished).

[15] Ariel Schwartzman, Meenakshi Narian, "Vertex fitting my means of the Kalman Filter Technique," D0 Note **3907** (2001) (Unpublished).

[16] B. Abbott *et al.* [D0 Collaboration], "Search for charge 1/3 third generation leptoquarks in p anti-p collisions at s**(1/2) = 1.8-TeV," Phys. Rev. Lett. **81**, 38 (1998). [arXiv:hep-ex/9803009].

[17] D. Hedin and V. Sirotenko, "Limits on the Production of Pair Produced third Generation Leptoquarks and ZX Events," D0 Note **3175** (1997) (Unpublished).

[18] T. Sjostrand et al., Computer Phys. Commun. 135 238 (2001).

[19] H.L. Lai et al., Eur. Phys. J C12, 375 (2000).

[20] http://www-clued0.fnal.gov/~nunne/cross-sections/nnlo_xsect.html

[21] N. Kidonakis and R. Vogt, Int. Mod. Phys. **A19** 1793 (2004).

[22] http://www-d0.fnal.gov/Run2Physics/top/d0_private/wg/singletop/singletop.html

[23] E.E. Boos, M.N. Dubinin, V.A. Ilyin, A.E. Pukhov, V.I. Savrin, *CompHEP: specialized package for automatic calculations of elementary particle decays and collisions,* SNUTP report 94-116, Seoul, 1994 (hep-ph/9503280).

[24] M.L Mangano et al., "ALPGEN, a generator for hard multiparton processes in hadronic collisions," JHEP 0307 (2003).

[25] M. Mangano, et. al., http://www-d0.fnal.gov/computing/MonteCarlo/generators/matching_prescriptions/mlm/mlm_prescription.html.

[26] B. Clément, Ph.D. thesis, Université Louis Pasteur, Strasbourg, N° d'ordre IPHC 06-004, N° d'ordre ULP 5086, FERMILAB-THESIS-2006-06 (2006).

[27] T. Junk, "Confidence level computation for combining searches with small statistics," Nucl. Instrum. Meth. A **434**, 435 (1999) [arXiv:hep-ex/9902006].

[28] S.Calvet, A. Duperrin, E Kajfasz, Search for Pair Production of Scalar Bottom Quarks with the D0 Detector in $p\bar{p}$ Collisions at $\sqrt{s} = 1.96$ TeV, D0Note **5074.** (2006) (Unpublished).

[29] T. Edwards *et. al.*, FERMILAB-TM-2278-E (2004).